

WIDEBAND OCEAN ALTIMETRY USING KU AND K-BAND SATELLITE SIGNALS OF OPPORTUNITY (SOOP)

by

Soon Chye Ho

A Dissertation

Submitted to the Faculty of Purdue University

In Partial Fulfillment of the Requirements for the degree of

Doctor of Philosophy



School of Aeronautics and Astronautics

West Lafayette, Indiana

May 2021

**THE PURDUE UNIVERSITY GRADUATE SCHOOL
STATEMENT OF COMMITTEE APPROVAL**

Dr. James L. Garrison, Chair

School of Aeronautics and Astronautics

Dr. Arthur E. Frazho

School of Aeronautics and Astronautics

Dr. Carolin Frueh

School of Aeronautics and Astronautics

Dr. Manuel Martín-Neira

ESA

Dr. Rashmi Shah

Jet Propulsion Laboratory

Approved by:

Dr. Gregory A. Blaisdell

TABLE OF CONTENTS

LIST OF TABLES	5
LIST OF FIGURES	6
LIST OF SYMBOLS	9
NOMENCLATURE	11
ABSTRACT	12
1 INTRODUCTION	14
1.1 Ocean Surface Topography Measurement	15
1.1.1 Remote Sensing Techniques for Measuring Altimetry Data	16
1.2 Motivation	17
2 LITERATURE REVIEW OF PRIOR WORK AND CURRENT ALTIMETRY RE- SEARCH	18
2.1 Literature Review	18
2.2 Signal Measurement	20
2.3 Properties Digital Communication Signals	20
3 SATELLITE ALTIMETRY	22
3.1 Basic Principle of Altimetry	22
3.2 Altimetry Measurement Over Ocean Surface	24
3.3 Orbit Determination	25
4 THEORY OF SIGNAL OF OPPORTUNITY AND REFLECTOMETRY	26
4.1 Characteristics of the Composite Signal	26
4.1.1 Correlation Properties	26
4.1.2 Altimetric Precision	28
4.1.3 Equivalent Noise Bandwidth	32
4.1.4 SNR of the Reflected SoOp	33

4.2	Cramer Rao Lower Bound Approach	36
4.2.1	General Gaussian CRLB	36
4.2.2	CRLB - Sample Independent Model	37
4.2.3	Root Mean Square Bandwidth	38
5	EXPERIMENTAL CAMPAIGN AT PLATFORM HARVEST	42
5.1	Instrument Overview	42
5.2	Experimental Campaign at Platform Harvest	44
5.2.1	In Situ Mean Sea Level for Data Comparison	45
6	ALTIMETRIC PRECISION MODEL EVALUATION USING KU-/K-BAND SIG- NAL OF OPPORTUNITY	49
6.1	Ku-/K-band Data Post-Processing	49
6.1.1	Data Processing	49
6.1.2	Experiment Result	50
	Signal to Noise Ratio	50
	Comparison to LiDAR	53
6.1.3	Analysis - Multiple Peaks (Ku-band RHCP)	54
6.1.4	Model Testing by Reducing Signal Bandwidth	59
7	ALTIMETRY PRECISION MODEL EVALUATION	64
7.1	Equivalent Noise Bandwidth	64
7.2	Cramer Rao Lower Bound	65
7.2.1	Model Performance and Result	66
7.3	Time Series K-Band RHCP Evaluation	68
7.3.1	Comparison between Model of Measured Data in Time Series.	72
7.4	Summary	74
8	CONCLUSION	77
	REFERENCES	79

LIST OF TABLES

4.1	Link budget of KU- and K-band SoOp Altimetry from fixed height and orbit . .	35
4.2	Link Budget for Spaceborne Ku-/ K-Band SoOp Altimetry	35
5.1	Parameter of Data Recording	45
6.1	Link Budget Ku and K -band SoOp Altimetry from Fixed height and Orbit . .	50
6.2	The comparison of standard deviation of Ku-/K-bands between theoretical and measurement result by using tide gauge	53
6.3	The comparison of standard deviation of Ku-/K-bands between theoretical and measurement result	53
6.4	The standard deviation of experimental data with different filter.	59
6.5	The standard deviation of experimental data with different bandwidth.	62
7.1	This table is the comparison of different method approach to compute the ENBW.	64
7.2	This table is the comparison of different model approach.	68
7.3	The RMS bandwidth and SNR of different section.	70
7.4	This table is the comparison of different model approach by different region of time.	70
7.5	This table is the comparison of different model approach. The data on the transition period are moved for K-RHCP measurement.	71

LIST OF FIGURES

2.1	The spectrum of Ku-band LHCP from DirecTV captured by spectrum analyzer. There are 16 channels each polarization. Each channel is approximately 25MHz.	21
2.2	The spectrum of K-band LHCP from DirecTV captured by spectrum analyzer. There are 12 channels each polarization. Each channel is approximately 36MHz.	21
3.1	Principle of Altimetry	24
4.1	The correlation waveform to measure the path delay between direct and reflected signal.	27
4.2	The geometry relationship between path delay and height of the receiver over sea surface	27
4.3	Determination of the rising time of the noisy pulse.	30
4.4	The figure showing the ENBW definition.	32
4.5	The triangle correlation waveform, the ratio of the peak power P_s and the corresponding slope is approximately inversely proportional to spectrum bandwidth.	38
4.6	This figure is the observed waveform (Blue) and the box filter (Red)	40
4.7	This figure is the Fourier transform of the box filtered correlation waveform. . .	41
5.1	Platform Harvest - The experimental site located at 10 km off the coast of central California near Point Conception. The receivers and equipment were located in the NASA JPL shed. The location of antennas is marked in the figure.	42
5.2	The direct and reflected antenna setup on the platform Harvest.	43
5.3	The integrated system of the Harvest experiment.	46
5.4	The time plan of signal recording.	47
5.5	Environmental Conditions during Experiment. Red markers are the time where multiple peaks appear in RHCP data as described in results section.	48
6.1	Time history of computed SSH(Ku-/K-band LHCP) after eliminating height bias vs. SSH measured by the tide gauge.	51
6.2	Scatter plot (Ku-/K-band LHCP) of computed SSH ($\sigma_H = 2.78$ cm) after eliminating height bias vs. SSH measured by the tide gauge.	52
6.3	Scatter plot (Ku-LHCP) of SoOp SSH vs. Lidar SSH for Ku-band LHCP and K-band RHCP/LHCP. Statistics are given in Table 6.3.	54
6.4	Scatter plot (Ku-band RHCP) of SoOp SSH vs. LiDAR SSH. After removing multiple peaks SSH data (marked in red and magenta), σ_H decreases to 5.89 cm	55

6.5	The waveform Power/Lag contour of Ku-RHCP showing effects of multipeak, x-axis: Time, y-axis: Lag(chip), Color-bar: post-correlation power waveforms $I^2 + Q^2$	56
6.6	Comparison between the correlation of co-polarization (RHCP★RHCP) and cross-correlation (RHCP★LHCP)	57
6.7	Environmental Conditions during the experiment. Red markers are the time where multiple peaks appear in RHCP data as described in results section. . . .	58
6.8	Platform Harvest under San Francisco and Los Angeles SpotBeam	59
6.9	The Power Spectrum Density of different filter. The result of the experiment data of different filter is shown in Table(6.4)	60
6.10	The power waveform of 2 channels and 8 channels filtering. The slope of the 8 channels wideband signal is steeper than power waveform of 2 channels.)	61
6.11	The spectrum by using resample function with 50 MHz (2 channels)	61
6.12	The Power Spectrum Density of different Bandwidth. The downsampling is using linear interpolation of the time series data we collect from the experiment. . . .	62
6.13	This graph shows the theoretical estimated precision and the experimental data	63
7.1	The Ku-LHCP spectrum and its ENBW.	65
7.2	The example of the measured correlation waveform and the parameters to estimate the precision.	66
7.3	The measured Ku-Band spectrum, the blue spectrum is single 4ms integration spectrum, the orange spectrum is the average of 1 sec of the measured spectrum.	67
7.4	The RMS bandwidth with/without beacon spike removal.	68
7.5	The RMS bandwidth of K-RHCP over recording time.	69
7.6	The normalized signal spectrum of K-RHCP of different region, divided into 5 periods	69
7.7	The RMS bandwidth vs Experiment Precision of K-RHCP over recording time.	71
7.8	The comparison between model prediction and measured precision of K-RHCP over region by region.	72
7.9	The RMS bandwidth model prediction vs Experiment Precision of KU-LHCP over recording time.	73
7.10	The General CRLB model prediction vs Experiment Precision of KU-LHCP over recording time.	73
7.11	The RMS bandwidth model prediction vs Experiment Precision of K-LHCP over recording time.	74

7.12	The General CRLB model prediction vs Experiment Precision of K-LHCP over recording time.	74
7.13	The RMS bandwidth model prediction vs Experiment Precision of K-RHCP over recording time.	75
7.14	The General CRLB model prediction vs Experiment Precision of K-RHCP over recording time.	75

LIST OF SYMBOLS

s_d	Direct Transmitted signal (GNSS, DTV etc)
S_r	Reflected signal from surface
ϕ	Random phase due to the different scattered surface
v_d	Output voltage from direct signal
v_r	Output voltage from reflected signal
n	Noise(Noise temperature, Antennna noise temperature)
T_c	Coherent time
f_0	Nominal center frequency
X	Cross correlation waveform
τ_p	Path delay with $ Z(\tau_p) ^2$ is maximum
f_D	Doppler frequency
θ	Elevation angle
P_s	Total reflected signal power of the surface
\bar{P}_s	Mean reflected signal power (assumed ergodic)
σ_s	STD of the signal power of the reflected surface
P_N	Noise power
\bar{P}_N	Mean noise power (assumed ergodic)
σ_N	STD of the noise power
SNR	Signal to noise ratio
H	Height measurement from sea surface to receiver
θ_{elev}	Elevation angle
σ_h	STD of the height estimation
B	Bandwidth
N_{INC}	Number of incoherent average
τ_r	Rising time of waveform
$ENBW$	Equivalent noise bandwidth
λ	Wavelength
σ_o	Scattering coefficient

G_r	Receiver gain
x	$x = Z(\tau_p) ^2$ Random variable x is the peak of the power waveform
$p(x : \tau_p)$	The pdf of x which parameterized by the parameter τ_p

NOMENCLATURE

ACF	Autocorrelation Function
ADC	Analog to Digital Convertor
CRLB	Cramer Rao Lower Bound
DDM	Doppler Delay Map
DFFT	Discrete Fast Fourier Transform
EIRP	Effective Isotropic Radiated Power
FFT	Fast Fourier Transform
GNSS	Global Navigation Satellite System
GNSS-R	Reflected - Global Navigation Satellite System
GPS	Global Positioning Satellite
ICF	Interferometric Complex Field
IF	Interferometric Frequency
IFFT	Inverse Fast Fourier Transform
LNB	Low Noise Block
LHCP	Left Handed Circular Polarization
LO	Local Oscillator
PDF	Probability Density Function
POD	Precise Orbit Determination
RF	Radio Frequency
RHCP	Right Handed Circular Polarization
RMS	Root Mean Square
SNR	Signal and Noise Ratio
SoOP	Signal of OPportunity
SSH	Sea Surface Height

ABSTRACT

Precise measurements of ocean parameters are important for atmospheric and weather modeling. Hence, several methods have been developed over recent decades, including altimetry, scatterometry, and radiometry for remotely sensing parameters like Significant Wave Height (SWH), Sea Surface Height (SSH), Mean Wave Period (MWP), Sea Surface Salinity (SSS), tidal level, wind speed, and wind direction. These techniques have been demonstrated during a series of satellite missions, including TOPEX/Poseidon, Jason, and QuickSCAT, evolving from “pathfinder” or demonstration experiments to operational missions. This dissertation explores a technique for measuring ocean surface topography parameters using reflectometry and telecommunication signals in a bistatic configuration.

This dissertation applies an ocean remote sensing method using Signals of Opportunity (SoOp), specifically reflected digital telecommunication satellite signals. The fundamental observation is the cross correlation waveform from the direct and reflected signal. Relationships are derived between the coherence time of the waveform and SSH of the sea surface. A proof-of-concept experiment has demonstrated that wideband (400 MHz) signals of opportunity (SoOp) transmitted in K and Ku-band from geostationary satellites can be used for coastal altimetry. An important finding from this experiment is that the full broadcast spectrum consisting of multiple digital channels can be processed as a single wideband signal source. An established error model for Global Navigation Satellite System interferometric altimetry (iGNSS-R) was shown to accurately represent the sea surface height (SSH) retrievals when evaluated using the full bandwidth. This experiment was conducted over a 72 hour period at Platform Harvest off the Pacific Coast. Co-located tide gauge and LiDAR measurements were used as in situ data. Two anomalies were observed in the experiment: 1. Multiple peaks in the cross correlation waveform from one polarization of Ku-band frequency. 2. Decrease in SNR from loss of a data channel. When the instances of multiple peaks were eliminated and the equivalent bandwidth recomputed using only the active channels, SSH error from these cases agreed well with the model prediction. Application of SoOp wideband altimetry will therefore require a monitoring capability to identify changes in the

transmission spectrum, total power, and waveform shape, for quality control and setting an appropriate observation error covariance. The measurement precision from a satellite receiver is predicted to be between 4-6 cm using the error model.

The last part evaluates the performance of altimetry measurements using the Cramer Rao Lower Bound and Root Mean Square bandwidth approaches. The full bandwidth model can well predict the overall precision of the path delay measurement in LHCP measurement. For K-RHCP measurement, after excluding the measurement data during spectrum transition period, the full bandwidth model can work well. SoOp altimetry with these signals may improve coastal measurements and increase the sampling and revisit rate through use of a constellation of small satellites.

1. INTRODUCTION

Atmospheric and weather modeling are important methods to generate forecasting and study of weather, climate. Accurate measurement of ocean parameters support storm surge prediction, development of realistic wave models, and improved forecasts of wave setup and overtopping processes [1]–[4]. In recent decades, the development of several methods, including altimetry, scatterometry, synthetic aperture radars and radiometry for remotely sensing parameters can accurately measure the ocean parameters like Significant Wave Height (SWH), Sea Surface Height (SSH), Mean Wave Period (MWP), Sea Surface Salinity (SSS), tidal level, wind speed, and wind direction. These techniques have been demonstrated on a series of satellite missions, including TOPEX/Poseidon [5], Jason-1 [6], Jason-2 [7] and QuickSCAT [8], evolving from “pathfinder” or demonstration experiments to operational missions. However, altimetry measurements have a limitation in coastal regions due to the land contamination, rapid tidal variation, and atmospheric effects.

Over the last two decades, ocean altimetry with Signal of Opportunity (SoOp) has been demonstrated using transmissions from the Global Navigation Satellite System (GNSS) [9]–[11]. Recently, techniques originally developed for GNSS have been applied to digital communication signals [12], [13] with the promise that wider bandwidth and higher power would enable sea surface height (SSH) retrievals at a scientifically useful precision [14]. The motivation for the experiment presented in this paper is to demonstrate the use of the full broadcast spectrum, consisting of multiple digital channels, as a single wideband source and to validate an established error model in this application. Application of the full (400 MHz) spectrum is required to achieve an SSH measurement precision in the centimeter range, which is scientifically useful.

This chapter delivers an overview of the importance of Ocean Surface Topography measurement in Section 1.1. Section 1.2 provides a review of the existing techniques to measure the key parameters for Ocean Topography analysis. The motivation for the research is described in Section 1.3. Lastly, an outline for the thesis will be in Section 1.4.

1.1 Ocean Surface Topography Measurement

The parameters of ocean surface topography (OST), including tides, circulation, and heat storage (absorption), are key measurements to help forecasting and study short-term changes in the weather, long-term climate patterns and to better understand of how the parameter changes could affect the environment. Besides, OST also has many other practical applications that affect our daily lives, such as offshore operations, ship navigation, and fisheries management.

Tides and currents are the two major factors that affect the dynamic topography of the ocean's surface. The water level change due to tides is the result of changes in the gravitational attraction of the sun and moon. The tides can be predicted by the astronomical tide model. Ocean currents are driven by the wind of the mixing of waters of different densities. The change of ocean surface level can vary from few centimeters to over a meter because of the moving bodies of water driven by ocean currents. These measurements of ocean surface level are important for scientific applications.

OST data is used in the wide-ranging of scientific applications. The OST data from altimetry instruments provides us a better understanding of the long-term global sea-level changes. Moreover, the altimetry data has also helped us to observe the fluctuation of El Nino, La Nina, and the Pacific Decadal Oscillation[15], [16]. The steric height changes from OST data is corresponds to the amount of heat stored in the upper layers of the ocean[17]. This information is useful in predicting hurricane season severity and forecasting individual storm severity. Therefore, altimetry OST data can provide information to the scientists to study these climate, weather, ocean circulation phenomena and better understand their impact on the environment and daily lives.

As a research tool, OST data also have many operational and practical applications, for instance, ship routing, offshore oil operations, recreational boating, fisheries management, and naval maritime operations. There are also land applications of OST data. Flood and drought can be investigated using the real-time data on the height of water in rivers and lakes. Additionally, the measurement of river level variations of the areas which are difficult to reach can also be made.

1.1.1 Remote Sensing Techniques for Measuring Altimetry Data

The major product of OST measurement is the sea surface height (SSH). The accuracy of in situ measurements using tide gauge or LiDAR is at the millimeter level. An altimeter, which is an active radar instrument, is an alternative way to measure the altitude of the ocean surface with respect to the geoid. In recent years, these altimeters have been deployed on satellites to measure SSH. There are altimeter satellites that have been operated for 20 years, include Geosat, Sentinel 3, TOPEX/Poseidon, Jason, European Remote Sensing (ERS) satellites [18].

Geosat (October 1985 -January 1990) - The US Geodetic Satellite was a pioneering research mission of the US Navy dedicated to radar altimetry. The primary mission (Geodetic Mission, GM) is dedicated to measuring the marine geoid at high resolution. The second mission phase is known as the "Exact Repeat Mission" (ERM). This mission provided more than three years of precise altimeter data. Geosat Follow-On (GFO) was launched on 10 February 1988 to continue ocean observation.

Sentinel 3 (February 2016 - present) - Sentinel 3 is an Earth Observation satellite mission developed by ESA as part of Copernicus. The major objective of Sentinel 3 mission is to measure sea-surface topography, sea and land surface temperature, and color with high-end accuracy to support ocean forecasting systems and climate monitoring.

TOPEX/Poseidon [5] (Sept 1992 - Oct 2005) - TOPEX/Poseidon (T/P) was the first altimetric mission jointly collaborated by NASA and CNES. T/P was capable of measuring significant wave height, atmospheric water vapor, and sea surface height. Jason-1 (Dec 2001 - June 2013) is a follow-on of T/P mission. Jason-1 measured the same parameters as T/P.

The altimetry data from the satellite altimeter are continually being used in data validation and calibration of sea surface height, wave height measurements. For global SSH measurement, Jason-2 can achieve SSH accuracy about 2.5 cm at a resolution of 300 m along-track at 20Hz and 7 km along-track at 1 Hz.

1.2 Motivation

The NASA/CNES Jason satellite, follow-on to the highly successful TOPEX/Poseidon mission, has continued to provide oceanographers and marine operators across the globe with a continuous, high-quality stream of sea surface height data for 12 years[18]. This unprecedented resource of valuable ocean data is being used to map sea surface height, geostrophic velocity, significant wave height, and wind speed over the global oceans. Altimeter data products are used by hundreds of researchers and operational users to monitor ocean circulation and improve our understanding of the role of the oceans in climate and weather.

Several challenges remain in the processing of the altimetric waveforms in the coastal zone, for instance, the correction of the measurements for path delay, contamination effects on waveforms due to land and bright targets, and revisit time resolution on coastal region[19]. Development of the technique to provide better accuracy and precision can assist scientists to characterize and predict the Earth system.

My research seeks to extend the applicability of the bistatic remote sensing - Global Navigation Satellite System Reflectometry (GNSS-R) to develop and evaluate a SoOp technique [9], [20], [21] with stronger power which includes a telecommunication satellite system. In addition, I am looking to develop an alternative approach for estimating the precision of the technique and evaluate the model by comparing it to the experimental results.

2. LITERATURE REVIEW OF PRIOR WORK AND CURRENT ALTIMETRY RESEARCH

This chapter gives the literature review of Altimetry is described in Section 2.1. Next, the fundamental measurement explored in this dissertation in Section 2.2. In section 2.3, a error model explanation and derivation of code altimetry in order to find the error in the precision of SSH estimation due to the measurement and instrument noise is presented.

2.1 Literature Review

Ocean remote sensing is an important technique for atmospheric and weather modeling. Several methods have been developed for remotely sensing ocean topography using microwave signals, including altimetry, scatterometry, and radiometry. The GNSS-R approach was first proposed in 1993 for satellite altimetry [9] and the bistatic radar of GNSS has been well developed in the last two decades. Since then, GNSS-R techniques have been extended to other applications in ocean remote sensing, which includes wind speed and significant wave height from various platforms [22],[10],[23].

The fundamental concept of GNSS-R is the correlation of the reflected signal with a replica of the broadcast signal, making use of the deterministic pseudo-random noise (PRN) contained in the modulation. The resulting cross-correlation vs. delay waveforms is then inverted to obtain an estimate of the ocean surface height. Furthermore, satellite altimetry combines precise orbit determination with accurate ranging by a microwave altimeter of the distance of ocean surface to the satellite, to determine the ocean surface height relative to a known reference surface or the center of the Earth. This method has been demonstrated to work well from air-borne or satellite platforms. From the first space-borne observation of an Earth-reflected GPS signal[10], the result is scaled to obtain the expected voltage signal-to-noise ratio (SNR) and altimetric accuracy for a generic GPS reflections altimetry mission. The estimated delay error is the function of SNR and the chip length. Moreover, mesoscale ocean altimetry continues to be a challenging area for satellite observations and of great interest for oceanographers trying to validate and drive their ocean circulation models with real

measurements. The Passive Reflectometry and Interferometry System (PARIS) using GNSS reflected signals was proposed as a means to perform ocean altimetry along several tracks simultaneously spread over a wide swath[24],[25]. PARIS proposes an altimetric instrument that exploits the full spectrum of GNSS signals for improved altimetric performance and provides multifrequency observations to correct for the ionospheric delay. Furthermore, an in-orbit demonstration mission proposes the proof of expected altimetric accuracy suited for mesoscale ocean science. The error of the height estimation can be simply obtained by translating the power uncertainty to a delay uncertainty. Thus, the power to delay uncertainty translation can be locally related to the first derivative of the power waveform. The altimetric precision of GNSS-R is limited by the relatively low power of transmitted signals and the full spectral bandwidth, the time-varying geometry of the navigation satellites, and the confinement of signal transmission to L-band. In contrast, digital communication satellites provide high-power broadcast signals, geostationary transmitters, and wide transmission bandwidth. [14] provides a proof-of-concept experiment and validation of an error model for bistatic altimetry using signals of opportunity (SoOps) and digital communication transmitted signal. The results of an estimation of the SSH using Ku-band, which is stronger in transmitted power, show the precision of estimation of height is better than what was found from the L-band global positioning system. [26],[27] present a prediction of the height precision of GNSS-R altimetry based on the statistical analysis of the well-known Cramer-Rao estimation bound (CRLB). Altimetric precision has been also derived by considering that both signal and noise are zero-mean Gaussian random variables and, in particular, by analyzing the full covariance matrix of the received signal. As expected, this method has provided worse performance than the previous one. This result is expected since the waveform samples are correlated [28]. Based on the CRLB method, the more the spectral energy is concentrated at the end of the band (away from the center frequency), the larger the second moment of the bandlimited signal spectrum will be. Thus, the precision of the time delay measurement will increase.

2.2 Signal Measurement

The reflected GNSS signals or digital communication signals can be used in a bistatic radar configuration for estimating the SSH. The output from the GNSS receiver is the delay-Doppler map (DDM) or waveform. The DDM or waveform is generated through the cross-correlation of a local copy of the PRN code with the reflected signal over increments in Doppler frequency equal to the pre-detection bandwidth. The output from the digital communication signal receiver is also the delay-Doppler map or waveform, but it is generated through the cross-correlation of a direct signal with the reflected signal. A peak of waveforms is used to compute the path delay. The fundamental measurement provided by the reflections is the path delay. This bistatic method essentially uses transmitters that are already available and hence operates at a low cost. An analytical model for the waveform requires a basic understanding of the properties of the digital communication signal. In the next section, Ku-band and K-band with two polarization from DirecTV will be discussed.

2.3 Properties Digital Communication Signals

DirecTV is an American direct broadcast satellite service provider that transmits signals in the Ku-band (12.2-12.7 GHz) and Ka-band (18.3- 19.8 GHz). They have multiple satellites located at 99° W (DirecTV 11), 101° W (DirecTV 4S), 103° W (DirecTV 10/12), 110° W (DirecTV 5), and 119° W (DirecTV 7S). These satellites are in geostationary orbit at an altitude of 35,888 km above the equator. The results presented in this dissertation are from the satellite located at 101° W (DirecTV 4S). Based on published information, the satellite located at 101° W transmits 32 different channels in the 12.224-12.676 GHz (Ku-Band) frequency range. Out of the 32 channels, 16 are right-hand circularly polarized (RHCP) and 16 are left-hand circularly polarized (LHCP) channels [29]. The polarization on the receiver is controlled by varying the voltage to the low noise block (LNB) of the antenna. The LNB, also, downconverts the signal from 12.2-12.7 GHz to 950-1450 MHz. The center frequency, bandwidth and the shape of the spectrum are shown in Figure(2.1) and Figure(2.2)

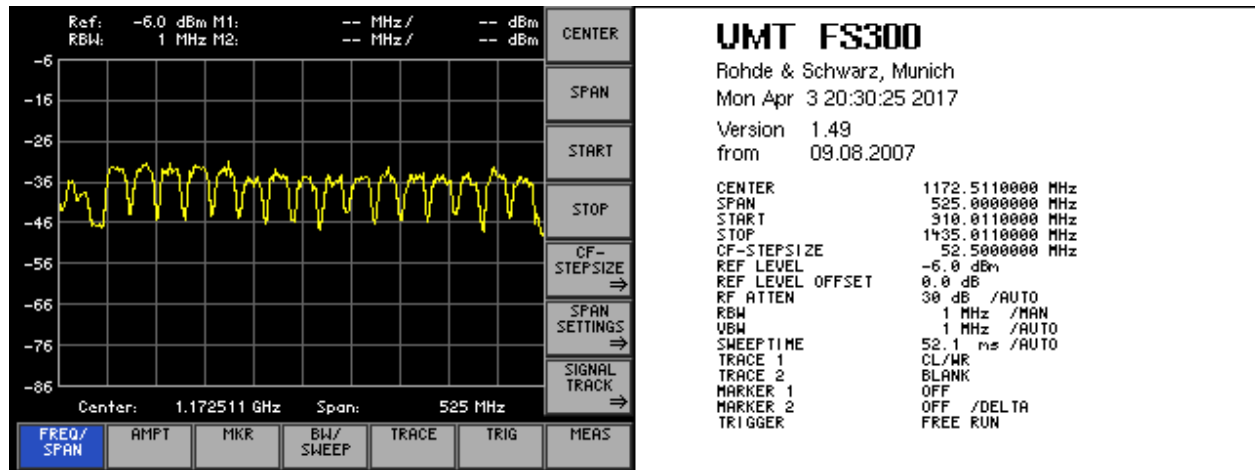


Figure 2.1. The spectrum of Ku-band LHCP from DirecTV captured by spectrum analyzer. There are 16 channels each polarization. Each channel is approximately 25MHz.

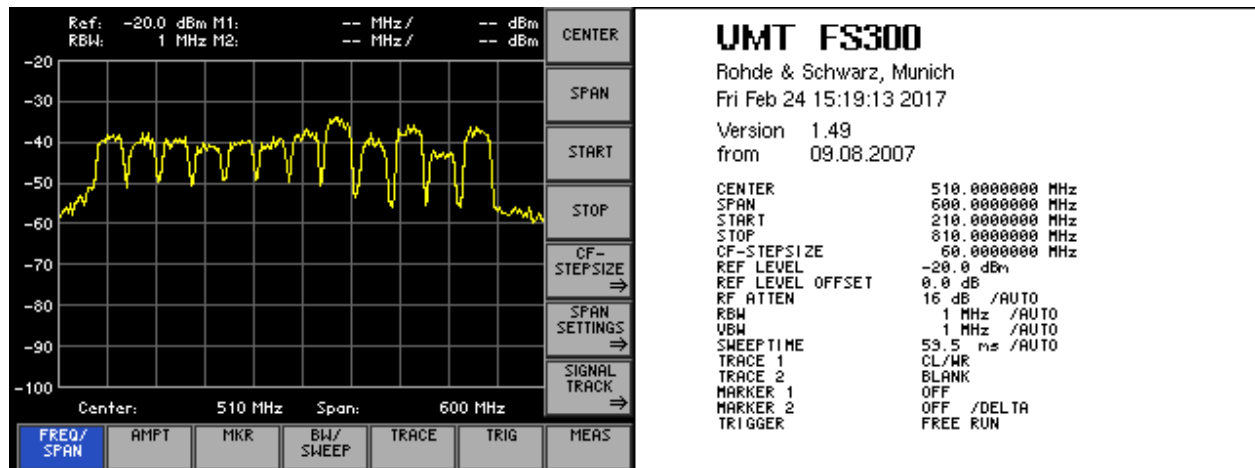


Figure 2.2. The spectrum of K-band LHCP from DirecTV captured by spectrum analyzer. There are 12 channels each polarization. Each channel is approximately 36MHz.

3. SATELLITE ALTIMETRY

An altimeter measures the reflected signal from the ocean surface and computes the distance of the satellite’s position on-orbit (concerning the reference ellipsoid) above the sea level (calculated by measuring the time taken for the signal to make the round trip). Besides surface height, the return signal’s amplitude and waveform can also be measuring wave height and wind speed over the oceans. The precise knowledge of the satellite’s orbital position is required to obtain measurements accurate to within a few centimeters over a range of several hundred kilometers. Thus the precise orbit determination systems are usually carried onboard altimetry satellites.

3.1 Basic Principle of Altimetry

Satellite-to-surface distance: Range

Radar altimeters onboard satellites transmit high-frequency signals to Earth and receive reflected signals from the surface and generate the observed waveforms. The observed waveforms are analyzed to derive a precise time measurement taken between the satellite and the surface. These time measurements can yield the range measurements. However, as high-frequency signals (as an electromagnetic wave) propagate through the atmosphere, and induce propagation speed change, which dependent upon water vapor or ionization. When these errors have been corrected, the range measurement can be estimated with great accuracy[30]. The independent measurements of the satellite’s orbital trajectory are necessary to measure surface height relative to a terrestrial reference ellipsoid.

Satellite Altitude

The critical orbital parameters for satellite altimeter missions are altitude, inclination, and period. The altitude of a satellite is the satellite’s distance for an arbitrary reference (e.g. the reference ellipsoid, a rough approximation of the Earth’s surface). The altitude of a satellite depends upon a number of constraints (e.g. inclination, atmospheric drag, gravity forces acting on the satellite, area of the world to be mapped, etc). The satellite can be

tracked in a number of ways to measure its altitude with the greatest possible accuracy and thus determine its precise orbit, accurate to within the order of a centimeter.

Surface Height

Altimetry is used to measure the altitude of the satellite above the closest point of the sea surface (Figure 3.1). Global precise tracking and orbit dynamic calculations can determine the height of the satellite above the ellipsoid, H , and the range from satellite to surface. The difference between these two measurements results in the sea surface height (SSH) given as:

$$SSH = H - R \quad (3.1)$$

For the ocean, the SSH integrates effects such as:

- The SSH would exist without any perturbing factors such as tides, wind, currents etc.), which is known as the geoid.
- The dynamic ocean topography (ocean circulation)
 - the permanent circulation induced by Earth's rotation, and permanent winds.
 - a highly dynamic component, for instance, sea surface wind, eddies, seasonal variations, etc.).

The better way to acquire the dynamic ocean topography is using the geoid height as a reference (Figure 3.1). In practical application, mean sea level is subtracted to compute the variable part of the ocean.

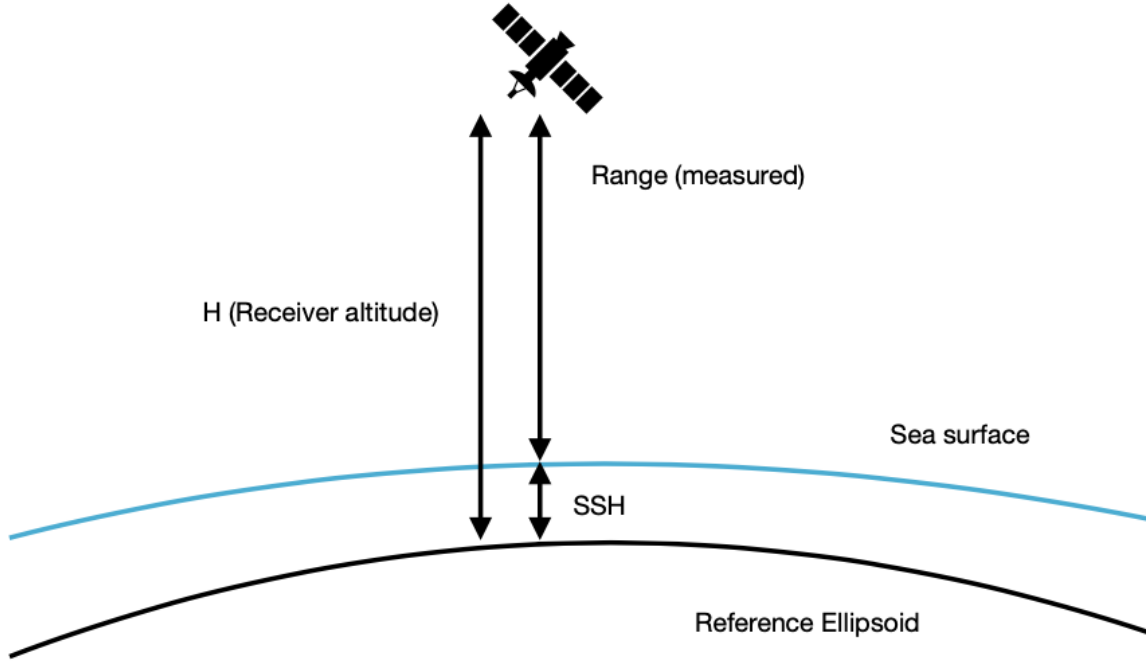


Figure 3.1. Principle of Altimetry

3.2 Altimetry Measurement Over Ocean Surface

When the sea surface is flat, the leading edge of the radar signal strikes the surface, and the amplitude of the reflected wave increases sharply. However, in rough seas, the amplitude of the reflected wave increase more moderately. Since the slope of the curve is proportional to wave height, we can compute ocean wave height from the waveforms of the reflected wave. The characteristic shape of the correlation can be analytically described from the Brown Model [31]. From the comparison of the averaged waveform with the theoretical, six parameters are discussed below:

- Epoch at mid-height: The time delay of the expected return of the radar pulse propagate between satellite-surface distance

- P: The amplitude of the useful signal. The emission amplitude provides the backscatter coefficient, σ_o
- Po: Thermal noise of the leading edge slope, which related to the significant wave height (SWH)
- Skewness: The curvature of the leading edge
- Trailing edge slope: Mispointing of the antenna.

3.3 Orbit Determination

Knowing the location of the altimeter antenna relative to the center-of-mass of the satellite, the altimeter range measurement can be used to determine the height of the ocean with respect to a reference surface. Variations in the ocean height of a few centimeters over length scales ranging from tens of kilometers to ocean basins must be accurately observed to utilize the altimeter data fully. To obtain the satellite height to this accuracy, precision orbit determination (POD) is introduced. POD is the procedure for determining the three-dimensional location of a satellite's center-of-mass (called the orbit ephemeris) at regularly spaced time intervals in a specified reference frame with high accuracy. To achieve one-centimeter orbit error, detailed information of the satellite and its orbital variations due to maneuvers, fuel consumption, solar panel orientation are needed. The forces (attraction, atmospheric drag, etc.) and the gravity field need to be precisely modeled and determined [18].

4. THEORY OF SIGNAL OF OPPORTUNITY AND REFLECTOMETRY

4.1 Characteristics of the Composite Signal

In this section, the analysis of the interferometric processing to produce the power waveform is reported. The interferometric processing consists of performing the complex cross-correlation between the received direct and reflected signals. When the correlation properties of the composite signal are analyzed, it allows accurate estimation of their relative delay between direct and reflected signals. In addition, in order to evaluate the ranging performance of the altimeter, it is fundamental to analyze the Signal to Noise Ratio (SNR) at the output of the cross-correlation. The SNR is a critical parameter for the interferometric processing configuration since it is affected by thermal noise at both up-looking and down-looking chains.

4.1.1 Correlation Properties

The model of the reflected signal is assumed to be the same as the model of the direct signal except for the time delay. An observation to be made is that in the model for peak delay presented here, the cross-correlation used to estimate the SSH is produced by a direct and reflected signal for a Signal of Opportunity (SoOp) signal under a finite integration time, T_I . The cross-correlation function is given by,

$$R(\tau, f_D) = \frac{1}{T_I} \int_0^{T_I} s_d(t) s_r^*(t - \tau) e^{-j2\pi f_D t} dt \quad (4.1)$$

where τ is the path delay between direct and reflected signal, f_D is the Doppler shift, $s_d(t)$ and $s_r(t)$ are the direct and reflected signals. The peak power along the τ axis is at the estimated path delay between direct and reflected signals. The example correlation waveform to estimate path delay is shown in Figure 4.1 The path delay, $\Delta\tau$ can be used to compute the distance between the receiver, h, and the sea surface. The geometry of the relationship between path delay and height of the receiver over sea surface is shown in Figure 4.2 The

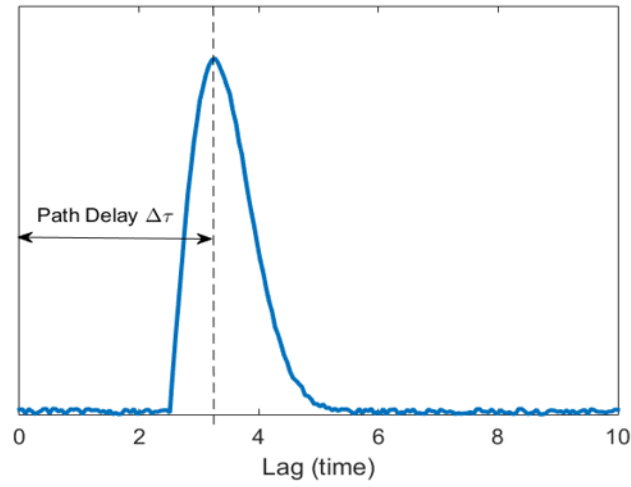


Figure 4.1. The correlation waveform to measure the path delay between direct and reflected signal.

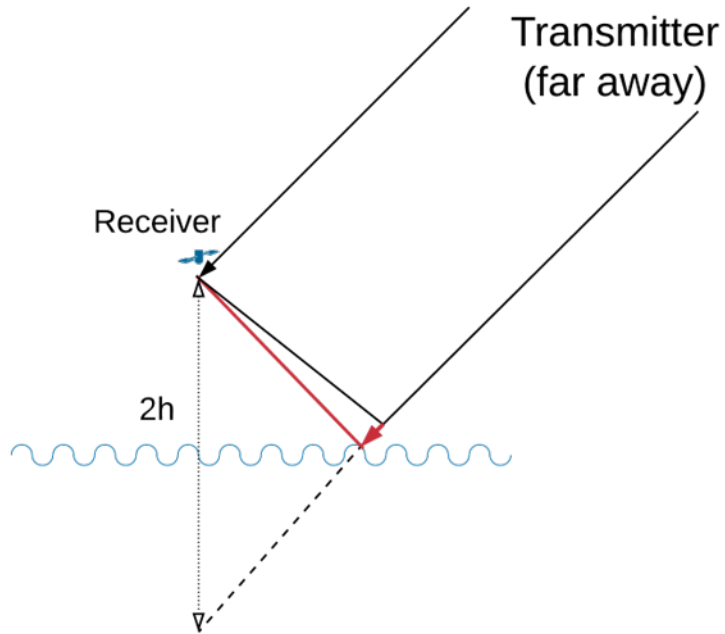


Figure 4.2. The geometry relationship between path delay and height of the receiver over sea surface

path delay, $\Delta\tau$, can be expressed as:

$$\Delta\tau = \frac{2h\sin(\theta)}{c} \quad (4.2)$$

where c is the speed of light, θ is the elevation angle. SSH can be computed by using h if the height of the receiver is known which make it applicable to ocean altimetry. The peak delay from the observed waveform is not the path delay at the specular reflection point since the roughness surface induces the scattered radiation field and affects the shape of the observed waveform and there is a change in both antenna patterns and free space loss across the chip-limited footprint. However, for a tower experiment, these errors induced are very small compared to the noise, which the receiver is at low altitudes. Moreover, the slope of the waveform is steeper for the wideband signal, the peak delay from the observed waveform can approximately be the specular path delay. The asymmetry induced by the roughness of the surface is hardly noticeable, and the footprint is so small that the free space loss change is negligible [24]. In addition, due to the narrow beamwidth of the antenna pattern, the trailing edge of the waveform is filtered, which is another reason why the asymmetry is hard to observe in the correlation waveform.

4.1.2 Altimetric Precision

This section is the review of the previous altimetry work. The altimetric precision is derived by theoretical signal model to compute the standard deviation of the peak delay from SNR and chip length. The received direct signal is represented as the sum of delay and attenuated version of the transmitted signal and the receiver thermal noise of the direct channel. The output voltage from direct and reflected signal can be written as:

$$v_d(t) = s_d(t) + n_d(t) \tag{4.3}$$

$$v_r(t) = s_r(t) + n_r(t) \tag{4.4}$$

The cross correlation of direct and reflected signal becomes[25],

$$\begin{aligned}
X(\tau) &= \frac{1}{T_I} \int_0^{T_I} v_d(t) v_r^*(t - \tau) dt \\
&= \frac{1}{T_I} \int_0^{T_I} s_d(t) s_r^*(t - \tau) dt + \frac{1}{T_I} \int_0^{T_I} s_d(t) n_r^*(t - \tau) dt \\
&+ \frac{1}{T_I} \int_0^{T_I} n_d(t) s_r^*(t - \tau) dt + \frac{1}{T_I} \int_0^{T_I} n_d(t) n_r^*(t - \tau) dt \\
&= X_{s_d s_r}(\tau) + X_{s_d n_r}(\tau) + X_{n_d s_r}(\tau) + X_{n_d n_r}(\tau)
\end{aligned}$$

By considering the transmitted signal and thermal noise are uncorrelated, the average power of the correlator output is the sum of four power terms,

$$\begin{aligned}
\langle |X(\tau)|^2 \rangle &= \langle |X_{s_d s_r}(\tau)|^2 \rangle + \langle |X_{s_d n_r}(\tau)|^2 \rangle + \langle |X_{n_d s_r}(\tau)|^2 \rangle + \langle |X_{n_d n_r}(\tau)|^2 \rangle
\end{aligned} \tag{4.5}$$

The average cross-correlation waveform power is the sum of the incoherent average of cross-correlated signal waveform power $\bar{P}_s = \langle |X_{s_d s_r}(\tau)|^2 \rangle$ and the average cross-correlated noise power terms $\bar{P}_N = \langle |X_{s_d n_r}(\tau)|^2 \rangle + \langle |X_{n_d s_r}(\tau)|^2 \rangle + \langle |X_{n_d n_r}(\tau)|^2 \rangle$. The Eqn can be rewritten as[25]:

$$\begin{aligned}
\bar{P}_R &= \langle |X(\tau)|^2 \rangle \\
&= \langle |X_{s_d s_r}(\tau)|^2 \rangle + \langle |X_{s_d n_r}(\tau)|^2 \rangle + \langle |X_{n_d s_r}(\tau)|^2 \rangle + \langle |X_{n_d n_r}(\tau)|^2 \rangle \\
&= \bar{P}_S + \bar{P}_N
\end{aligned} \tag{4.6}$$

The total reflected power \bar{P}_R can be written as the function of signal power \bar{P}_s and the $SNR = \frac{\bar{P}_S}{\bar{P}_N}$,

$$\begin{aligned}
\bar{P}_R &= \bar{P}_S + \bar{P}_N \\
\bar{P}_R &= \bar{P}_S \left(1 + \frac{\bar{P}_N}{\bar{P}_S} \right)
\end{aligned} \tag{4.7}$$

$$\bar{P}_R = \bar{P}_S \left(1 + \frac{1}{SNR} \right) \tag{4.8}$$

Since the mean of the power is equal to the standard deviation of the power[32], the standard deviation of total reflected power can be written as:

$$\sigma_R = \frac{\bar{P}_S}{\sqrt{N_{INC}}} \left(1 + \frac{1}{SNR}\right) \quad (4.9)$$

correspondingly, the noise power standard deviation becomes,

$$\sigma_N = \frac{\bar{P}_S}{\sqrt{N_{INC}}} \frac{1}{SNR} \quad (4.10)$$

Since the signal and noise are uncorrelated, the standard deviation in the useful power is the sum of the root-mean-square,

$$\sigma_S = \sqrt{\sigma_R^2 + \sigma_N^2} \quad (4.11)$$

$$= \frac{\bar{P}_S}{\sqrt{N_{INC}}} \sqrt{\left(1 + \frac{1}{SNR}\right)^2 + \left(\frac{1}{SNR}\right)^2} \quad (4.12)$$

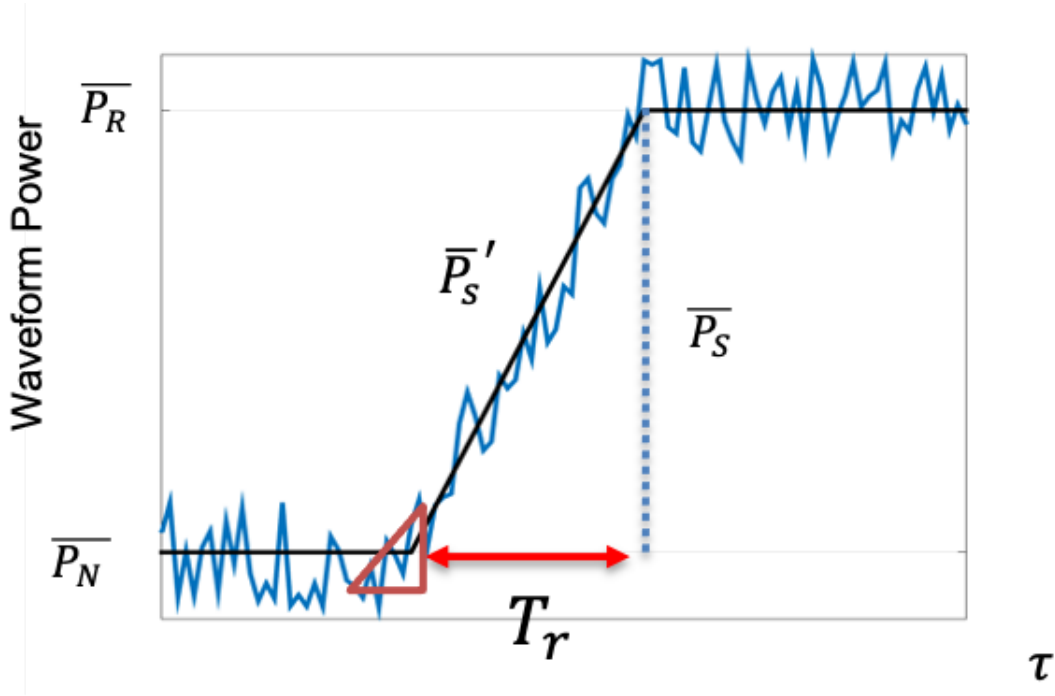


Figure 4.3. Determination of the rising time of the noisy pulse.

The accuracy of the path delay estimation can be simply obtained by converting the power uncertainty to a delay uncertainty. The power and delay uncertainty translation can be computed by using the local first derivative of the tracking point of the power waveform. The standard deviation of the path delay can be expressed as[25]:

$$\sigma_S = \frac{\bar{P}_S}{\bar{P}_S \sqrt{N_{INC}}} \sqrt{\left(1 + \frac{1}{SNR}\right)^2 + \left(\frac{1}{SNR}\right)^2} \quad (4.13)$$

In Figure(4.3), the ratio of $\frac{\bar{P}_S}{P_S}$ can be computed by the rising time T_r of the received pulse or chip length of the given signal. The standard deviation of path delay estimation would becomes:

$$\sigma_{\tau_r} = \frac{t_r}{\sqrt{N_{INC}}} \sqrt{\left(1 + \frac{1}{SNR}\right)^2 + \left(\frac{1}{SNR}\right)^2} \quad (4.14)$$

By considering the geometric relationship between height and path delay, the precision of height estimation would become:

$$\sigma_H = \frac{cT_r}{2\sin\theta\sqrt{N_{INC}}} \sqrt{\left(1 + \frac{1}{SNR}\right)^2 + \left(\frac{1}{SNR}\right)^2} \quad (4.15)$$

The rising time, T_r , which can also be the chip length of the given signal, can be approximate as $\frac{1}{B}$, where B is the signal bandwidth. Hence, the standard deviation of height can be rewritten as:

$$\sigma_H = \frac{c}{2B\sin\theta\sqrt{N_{INC}}} \sqrt{\left(1 + \frac{1}{SNR}\right)^2 + \left(\frac{1}{SNR}\right)^2} \quad (4.16)$$

The SNR is directly proportional to the cross-correlation integration time T_I and antenna gain. In Eqn(4.16), a high SNR is necessary to reduce the standard deviation. However, it is not a sufficient parameter to achieve submesoscale altimetry precision. In other words, even for infinite SNR, the height precision is not sufficient when incoherent averaging is not performed. Secondly, the number of waveform samples, N_{INC} , for incoherent averaging can also greatly reduce the standard deviation of height estimation. However, the N_{INC} cannot be increased without limit since the spatial resolution will degrade when the number of incoherent averaging increases. For submesoscale altimetry (10 km), the spatial resolution requirement is limited, N_{INC} will not be the key parameter to improve height precision.

Furthermore, the height precision is inversely proportional to the signal bandwidth, ‘ B ’. Hence, exploiting the wideband signals can maximize the height precision.

4.1.3 Equivalent Noise Bandwidth

Previously, the error model has been derived (Eqn(4.16)). The signal bandwidth, B , can be used in the model. Alternatively, since the spectrum of the wideband signal consists of multiple channels, we can use the Equivalent Noise Bandwidth (ENBW) to compute the effective bandwidth and apply it in Eqn(4.16).

Equivalent noise bandwidth is defined as the bandwidth of a brickwall filter that produces the same integrated noise power as that of an actual filter. This is also referred to as noise bandwidth or effective noise bandwidth. In Figure(4.4), the ENBW is equal area under the signal spectrum.

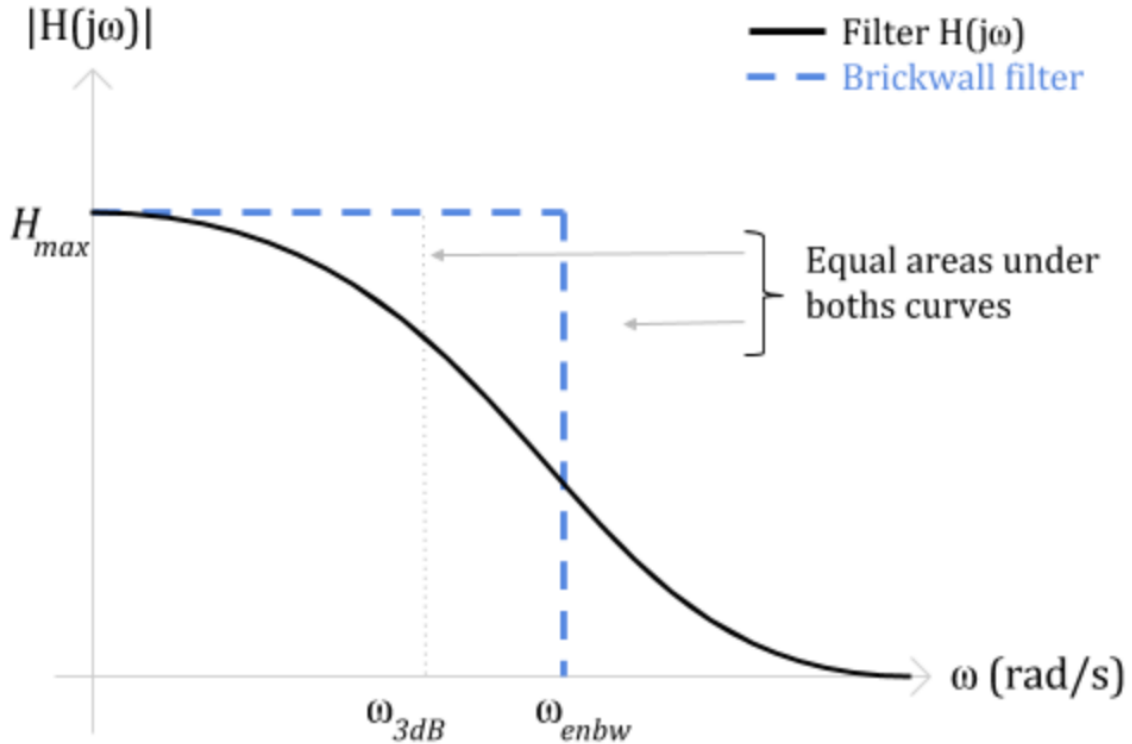


Figure 4.4. The figure showing the ENBW definition.

4.1.4 SNR of the Reflected SoOp

Since SNR is one of the key parameters to compute the precision of height estimation, we need to calculate the theoretical SNR of the signal and also compare it to the experimental measurement. The SNR can be computed by using a bistatic radar equation. The received signal is modeled by the sum of multiple independent scatters from the ocean surface. The amplitude α_k is the square root of the scattered power, P_k , which is given by the radar equation[33],

$$P_k = \frac{P_t G_t}{4\pi s^2} \frac{\sigma_o A_k}{4\pi r^2} \frac{\lambda^2 G_r}{4\pi} \quad (4.17)$$

where P_t is the transmitted power, G_t and G_r is the antenna gain of each transmitter and receiver, s and r are the distance from transmitter and receivers to each scattering element, σ_o is the scattering coefficient, A_k is the area of each scattering element. The scattered signal can be modeled as the superposition of the returns from many elements, each with different time delay τ_k , phase ϕ_k , and amplitude α_k , therefore we write the received electric field as

$$E = \sum_k \alpha_k e^{-j(\frac{2\pi c}{\lambda} \tau_k + \phi_k)} \quad (4.18)$$

where c is the speed of light and λ is the carrier wavelength. When correlating the received reflected signal with a model signal of delay τ_m and phase ϕ_k , and integrating over a few milliseconds, the correlation function is approximately a triangle function, $\Lambda(\tau_m - \tau_k)$ [34] multiplied by the amplitude α_k and the phasor $e^{-j(\phi_m - \phi_k)}$. When the surface is rough, because of superposition, each term in Eqn 4.18 contributes to the correlation function to give

$$R_p(\tau_m) = \sum_{k=1}^{\infty} \alpha_k e^{j(\tau_m - \tau_k)} \Lambda(\tau_m - \tau_k) \quad (4.19)$$

Squaring R_p and taking the ensemble average, the cross-terms from different scatterers to be cancelled due to the assumption of incoherent scattering.

$$\langle R_p R_p^* \rangle(\tau_m) = \sum_{k=1}^{\infty} \frac{P_t G_t}{4\pi s^2} \frac{\sigma_o}{4\pi r^2} \frac{\lambda^2 G_r}{4\pi} A_k \sigma_{o_k} \Lambda^2(\tau_m - \tau_k) \quad (4.20)$$

The total reflected power, P_s , can be integrated from finite sum of A_k to integral over the scattering surface and the equation is shown below[21],

$$P_s = \frac{P_t G_t}{4\pi s^2} \frac{\sigma_o}{4\pi r^2} \frac{\lambda^2 G_r}{4\pi} \int \int_A \Lambda^2(\tau - \tau_{x,y}(x, y)) dx dy \quad (4.21)$$

In order to compute theoretical reflected power, the majority power is assumed from the specular point which is valid for tower experiment. The scattering coefficient is assumed 11 dB, which corresponds to 7 km/s average sea surface wind speed.

The antenna gain can be computed by using the antenna gain equation, $G = \frac{\pi^2}{\theta_{3dB}}$, of parabolic dish where θ_{3dB} is the beamwidth in radians. The beamwidth can be computed by using $\theta_{3dB} = \frac{70\lambda}{D}$ in degree where D is the dish diameter in meters and λ is the wavelength.

The noise can be computed by: $N_0 = k_B T$ is Boltzmann's constant, and T is the noise temperature of the system. The post correlation SNR can be computed by adding processing gain, which is the multiple of signal bandwidth and coherent integration time. The post-processing SNR of the Harvest Experiment is shown in Table.4.1 In addition, we can extend the same concept to spaceborne system and the link budget calculation is shown in Table.4.2.

Table 4.1. Link budget of KU- and K-band SoOp Altimetry from fixed height and orbit

	KU-Band	K-Band	Unit
Transmitter Height	36000	36000	km
Receiver Height	28.2	28.2	m
EIRP $P_t G_t$	50	50	dBW
Path Loss $(4\pi s^2)^{-1}(4\pi r^2)^{-1}$	-201.7	-201.7	dB
Isotropic antenna effective area $(\frac{\lambda^2}{4\pi})$	-43.2	-46.9	dBm^2
Antenna Gain G_r	33.5	33.5	dBIC
Scattering cross section, σ_o	11	11	dB
Received Signal Power, P_s	-139.73	-151.3	dBW/Hz
Noise, kTB_N	-118.2	-118.2	dBW/Hz
Pre-Correlation, S/N	-21.5	-24.9	dB
Processing Gain, G_p	62	62	dB
Post-Correlation, SNR	40.95	37.58	dB

Table 4.2. Link Budget for Spaceborne Ku-/ K-Band SoOp Altimetry

	Value	Value	Units
Transmitter Height	36000	36000	km
Receiver Height	1380	500	km
EIRP, $P_t G_t$	50	50	dBW
Path loss, $(4\pi s^2)^{-1}(4\pi r^2)^{-1}$	-295.8	-287.1	dB
Isotropic antenna effective area $(\lambda^2/4\pi)$	-43.2	-43.2	dBm^2
Antenna gain, G_r	33.5	33.5	dBIC
Surface Area of Reflection , $\int \int dx dy$	68.1	63.7	dB
Scattering cross section, σ_0	11	11	dB
Received Signal Power, P_s	-176.6	-172.2	dBW
Noise, kTB_N	-117.9	-117.9	dBW/Hz
Pre-Correlation, S/N	-58.7	-54.2	dB
Processing Gain, G_P for $T_I=4$ ms	62.0	62.0	dB
Post-Correlation, SNR	3.4	7.8	dB
Averaging Time	1	1	sec
SSH Precision	5.3	4.1	cm

4.2 Cramer Rao Lower Bound Approach

In the previous section, the rising time, t_r , of the power waveform can be approximately computed by the signal bandwidth. Since one of the applications of signal processing of Cramer Rao Lower Bound theory is the range estimation of the radar[35], in this section, the CRLB approach will be discussed and apply to the wideband signal altimetry problem. Cramer Rao lower Bound can place a lower bound on the variance of any unbiased estimator and allows to predict the performance of an estimator when the observation can be modeled as a probability density function. In this section, the measured waveform is proposed to derive the CRLB for expected altimetry performance. First, the general Gaussian expression for CRLB is derived which assumes that both the mean and covariance depend on the parameter. Second, the simplified approach, which considering the covariance is not dependent on the parameter ($C = \sigma^2 * I$), is derived.

4.2.1 General Gaussian CRLB

The correlation waveform is the production of the correlation of direct and reflected output voltage (complex voltage). The observed waveform can be written as: $\mathbf{y} \sim N(\mu_y(\tau_p), C(\tau_p))$ where $\mathbf{y} = V_x + jV_y$. V_x and V_y are the component of the complex voltage. $C(\tau_p)$ is the covariance matrix (Hermitian matrix). The mean $\mu_y(\tau_p) = E(V_x) + jE(V_y)$. The complex Gaussian probability density function (pdf) can be written as:

$$p(\mathbf{y}; \tau_p) = \frac{1}{(2\pi)^{N/2} |C(\tau_p)|^{1/2}} \exp[(\mathbf{y} - \mu_y(\tau_p))^H C^{-1}(\tau_p) (\mathbf{y} - \mu_y(\tau_p))] \quad (4.22)$$

By applying the following matrix identities (Eqn 4.23, Eqn 4.24)

$$\frac{d \ln |C(\tau_p)|}{d\tau_p} = \text{trace} \left(C^{-1}(\tau_p) \frac{dC(\tau_p)}{d\tau_p} \right) \quad (4.23)$$

$$\frac{dC^{-1}(\tau_p)}{d\tau_p} = -C^{-1}(\tau_p) \frac{dC(\tau_p)}{d\tau_p} C^{-1}(\tau_p) \quad (4.24)$$

We can obtain the Fisher Information, Eqn 4.25

$$I(\tau_p) = E \left[\left(\frac{d \ln(p(\mathbf{y}; \tau_p))}{d\tau_p} \right) \left(\frac{d \ln(p(\mathbf{y}; \tau_p))}{d\tau_p} \right) \right] \quad (4.25)$$

Since τ_p is a scalar parameter, $I(\tau_p)$ will reduce to,

$$I(\tau_p) = \frac{1}{2} \text{tr} \left[\left(C^{-1}(\tau_p) \frac{dC(\tau_p)}{d\tau_p} \right)^2 \right] + \left(\frac{d\mu_y(\tau_p)}{d\tau_p} \right)^H C^{-1}(\tau_p) \left(\frac{d\mu_y(\tau_p)}{d\tau_p} \right) \quad (4.26)$$

4.2.2 CRLB - Sample Independent Model

In this section, x is the peak power waveform and sampled peak power waveform is assumed to be independent, the covariance matrix, C , of the waveform $x(\tau_p)$ is the variance of the peak power waveform, with the speckle noise σ_s ($C(\tau_p) = \sigma_s^2 I$). The first term of Eqn 4.26 will be zero and the Fisher Information Matrix reduces to,

$$I(\tau_p) = - \frac{\left(\frac{d\mu(\tau_p)}{d\tau_p} \right)^2}{\sigma_s^2} \quad (4.27)$$

The variance of the estimator $\hat{\tau}_p$ becomes:

$$\text{var}(\tau_p) \geq \frac{\sigma^2}{\left(\frac{d\mu(\tau_p)}{d\tau_p} \right)^2} \quad (4.28)$$

To evaluate the $\text{var}(\tau_p)$, we need to compute the variance of the noise from both the fading speckle and the thermal noise. The denominator $\frac{d\mu(\tau_p)}{d\tau_p}$ is the local gradient of the peak waveform power. the overall standard deviation of the τ_p estimation can be written as the root mean square of both components,

$$\sigma_{\tau_p} \geq \frac{P_s}{\sqrt{N_{INC}} \left(\frac{\partial \mu(\tau_p)}{\partial \tau_p} \right)} \sqrt{\left(\left(1 + \frac{1}{SNR} \right)^2 + \left(\frac{1}{SNR} \right)^2 \right)} \quad (4.29)$$

P_s is the peak power waveform, the unit is W. The local gradient of the peak power waveform $\frac{d\mu(\tau_p)}{d\tau_p}$ and the unit is W/s. When the main peak of the correlation waveform is approximately the triangle function (Figure 4.5), the ratio of the maximum power P_s and

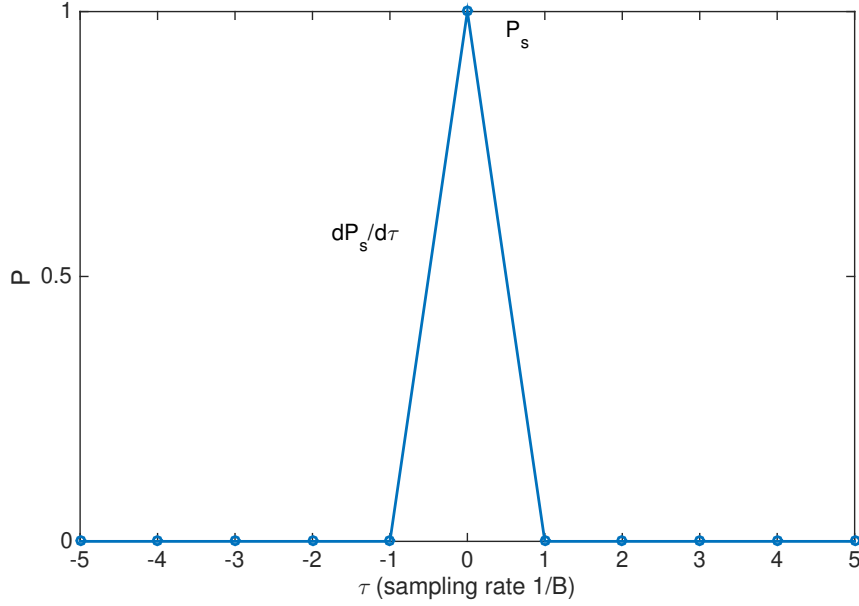


Figure 4.5. The triangle correlation waveform, the ratio of the peak power P_s and the corresponding slope is approximately inversely proportional to spectrum bandwidth.

the slope of the estimator path delay $\frac{d\mu(\tau_p)}{d\tau_p}$, can approximately be the raising time, T_r , which shown in Eqn(4.16). These two models could lead to the same result and τ_r is inversely proportional to the signal bandwidth, B.

When the main peak of the correlation waveform is approximately the triangle function (Figure 4.5), the ratio of the maximum power P_s and the slope of the estimator path delay $\frac{dx}{d\tau_p}$, can be approximately as the rising time, T_r , which shown in Eqn 4.16. These two models could lead to the same result and τ_r is inversely proportional to the signal bandwidth, B.

4.2.3 Root Mean Square Bandwidth

From Eqn 4.29, the peak power of the power waveform \bar{P}_s can be computed by the zero moment of power spectrum (Eqn.4.30), m_o , by using the Parseval theorem[27] [26]. By using the Fourier transform and the Parseval theorem, the first derivative of the entire

power waveform can be computed by using the second moment, m_2 , of the power spectrum (Eqn.4.31).

$$m_0 = \int_{-\infty}^{\infty} |X(f)| df \quad (4.30)$$

$$m_2 = \int_{-\infty}^{\infty} f^2 |X(f)| df \quad (4.31)$$

where f denotes continuous time frequency, and $X(f)$ is the Fourier Transform of the cross correlation waveform, $x(\tau)$. The ratio of the maximum power \bar{P}_s and the slope of the estimator path delay $\frac{dx}{d\tau_p}$, can be alternatively computed by the ratio of the second and zero moment of the spectrum, $\frac{m_2}{m_0}$, which is called Root Mean Square Bandwidth or Gabor Bandwidth. The root mean square bandwidth can be written as[27][26]:

$$B_{rms}^2 = \frac{\int_{-\infty}^{\infty} f^2 |X(f)| df}{\int_{-\infty}^{\infty} |X(f)| df} \quad (4.32)$$

Taking Eqn(4.30) and (4.31) into Eqn(4.29), we can rewrite the standard deviation as:

$$\sigma_{\tau_p}^2 \geq \frac{1}{N_{INC}(2\pi B_{rms})^2} \left(\left(1 + \frac{1}{SNR}\right)^2 + \left(\frac{1}{SNR}\right)^2 \right) \quad (4.33)$$

The standard deviation of the height estimation can be obtained by translating the power uncertainty to a path delay uncertainty. The height precision σ_h can be expressed as follows:

$$\sigma_h \geq \frac{c}{\sin(\theta)\sqrt{N_{INC}}} \frac{1}{(2\pi B_{rms})} \sqrt{\left(\left(1 + \frac{1}{SNR}\right)^2 + \left(\frac{1}{SNR}\right)^2 \right)} \quad (4.34)$$

The difference between using RMS bandwidth of the spectrum and power waveform to estimate the precision is that the RMS bandwidth of the spectrum considers the full power waveform of the cross correlation and the power waveform only considers the local gradient of the peak power waveform.

Modified Root Mean Square Bandwidth

The root mean square bandwidth considers the full spectrum (Fourier transform of the full waveform), however, the path delay estimation is computed from peak power waveform.

In Figure(4.6), the correlation power waveform has multiple peaks. since we only use the peak power to estimate the path delay, the box filter can be applied in the correlation waveform to filter the irrelevant side peaks. The filtered power spectrum can be used to compute the RMS bandwidth to estimate the altimetry precision.

$$w(\tau_p) = 1 \quad (\tau_p \pm \Delta\tau_p) \quad (4.35)$$

$$= 0 \quad (otherwise) \quad (4.36)$$

$$x_f(\tau_p) = x(\tau_p) * w(\tau_p) \quad (4.37)$$

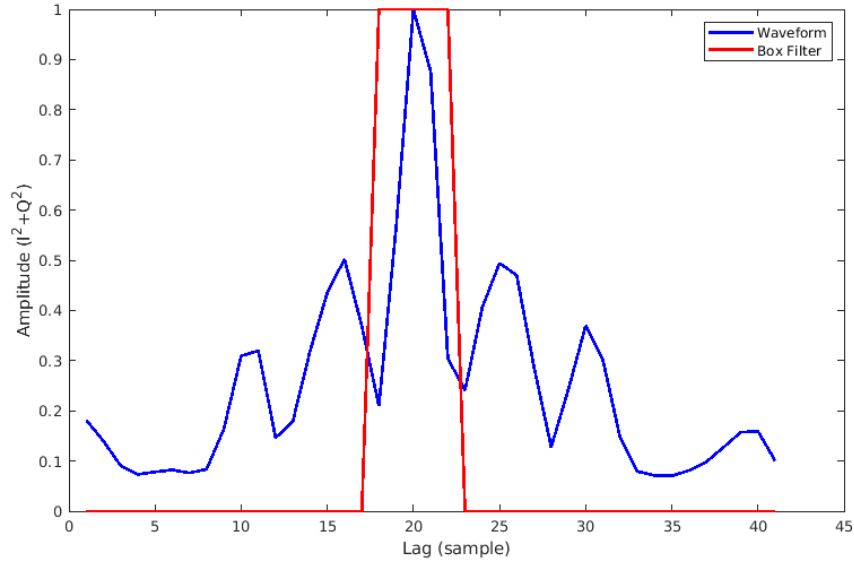


Figure 4.6. This figure is the observed waveform (Blue) and the box filter (Red)

$$X_f(f) = \int_0^{T_i} x_f(\tau_p) e^{-j2\pi f \tau_p} d\tau_p \quad (4.38)$$

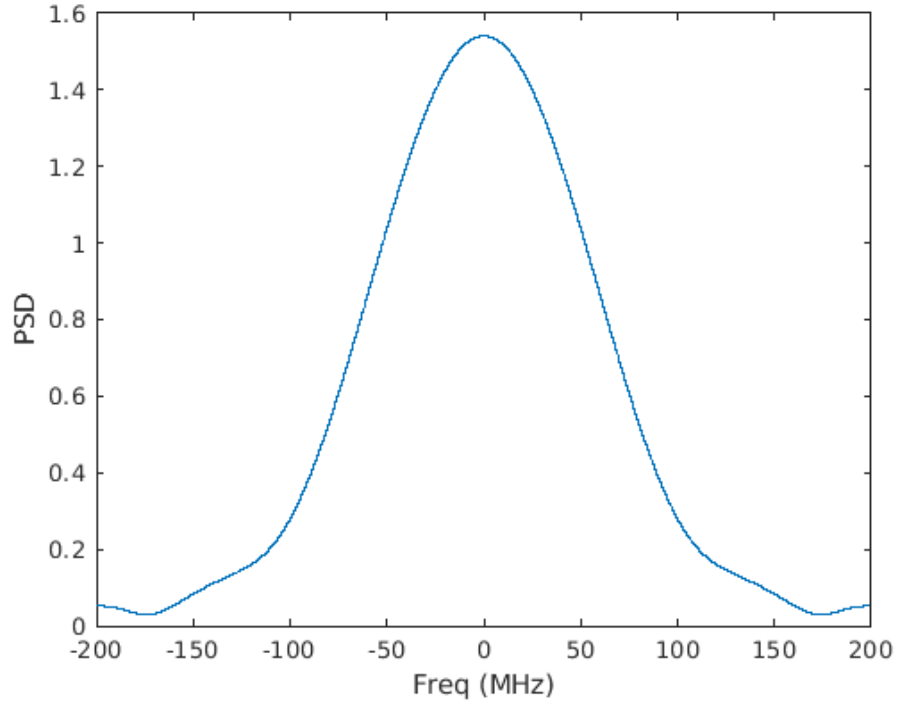


Figure 4.7. This figure is the Fourier transform of the box filtered correlation waveform.

The RMS bandwidth of the filter spectrum can be computed by:.

$$B_{f_{rms}}^2 = \frac{\int_{-\infty}^{\infty} f^2 |X_f(f)| df}{\int_{-\infty}^{\infty} |X_f(f)| df} \quad (4.39)$$

5. EXPERIMENTAL CAMPAIGN AT PLATFORM HARVEST

This chapter describes the experimental campaign setup at Platform Harvest in order to verify the SSH retrieval model.

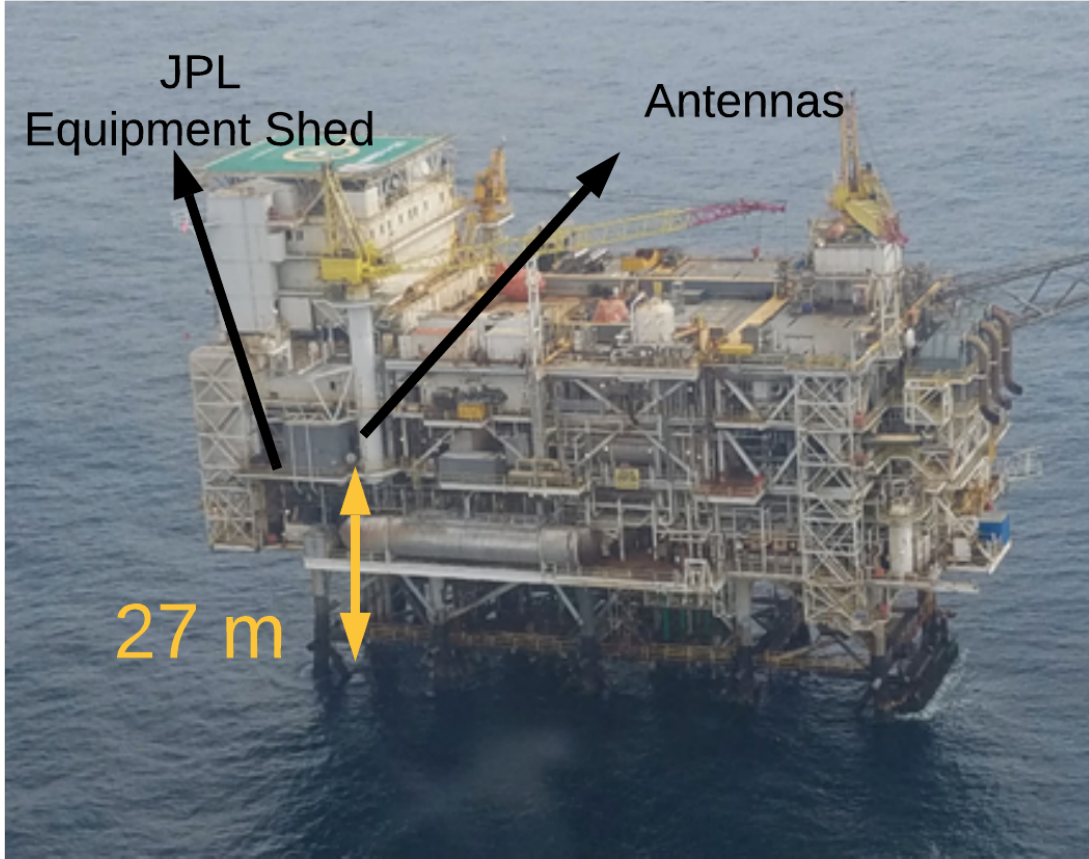


Figure 5.1. Platform Harvest - The experimental site located at 10 km off the coast of central California near Point Conception. The receivers and equipment were located in the NASA JPL shed. The location of antennas is marked in the figure.

5.1 Instrument Overview

Two different wideband signals were recorded during the experimental campaign to evaluate the precision on SSH measurement. This section is the overview of the instruments



Figure 5.2. The direct and reflected antenna setup on the platform Harvest.

which were used to record the direct and reflected signal for each of the wideband signals from the DirecTV satellite.

DirecTV is a Direct Broadcast System (DBS) service provider in the United States that occupies two 500 MHz frequency blocks in Ku (12.2-12.7 GHz) and K-band (18.3-18.8 GHz). The DBS signal is composed of 24 MHz channels in Ku-band and 36 MHz channels in K-band with some gaps between the channels. Both Left Hand Circularly Polarized (LHCP) and Right Hand Circularly Polarized (RHCP) signals are broadcast in each band.

We designed an instrument to capture direct and reflected signals from both DirecTV bands. A block diagram of this instrument is shown in Figure 5.3. Commercial “Slimline” satellite dishes (SL5K4NR0-02) with gains of 33.5 dB and two outputs were used to capture the signals. These antennas have built-in Low Noise Block (LNB) downconverters driven by independent local oscillators (LO) that downconvert Ku-band to 950-1450 MHz and K-band to 250-750 MHz intermediate frequencies. A frequency bias (f_D), due to independent LOs, will be present in the Doppler dimension when the direct and reflected signals are cross-

correlated. In order to estimate and remove this frequency bias, a signal generator (referred to as beacon) was installed to emit coherent 18.65 GHz (K-band) and 12.65 GHz (Ku-Band) tones into each antenna. The azimuth and elevation angle of the antennas were fine-tuned using a signal strength meter to receive both Ku- and K-band signals simultaneously. Figure 5.2 shows the antenna installation at Platform Harvest.

A commercially available device, known as a “polarity locker” (Sonora Design 4SATPL-T) was used to select the band and polarization for each antenna: Ku/K-band LHCP and Ku/K-band RHCP. Two outputs of the antennas were connected to two inputs of the polarity lockers. Line amplifiers (Sonora Design LA144R-T) were placed after the polarity lockers. The incoming intermediate frequency (IF) signal was then processed through a second IF Front End and converted to baseband. The Reconfigurable Open Architecture Computing Hardware (ROACH2) [36], was used to digitize and record the baseband signal. ROACH2 is an open-source platform with a field programmable gate array (FPGA) capable of recording two 400 MHz signals simultaneously. ROACH2 records 2×2^{20} bytes samples (5.24 ms) in a burst, followed by a 215 ms data writing interval.

Every hour, 1414 bursts, equivalent to 7.24 seconds of direct and reflected data, are recorded. A Ku/K-band switch in the IF front end was used to switch between Ku-band and K-band every 6 minutes during recording, Ku and K-band were recorded successively. Figure 5.4 shows a diagram illustrating this timing.

5.2 Experimental Campaign at Platform Harvest

The SSH experimental campaign was conducted at Platform Harvest which is located at 34.469°N, 120.682°W and which is about 10 km off the coast of central California near Point Conception. Since Platform Harvest is a “calibration site” for Jason-1 and TOPEX/POSEIDON missions, this site was been selected to perform SSH experiments to test and verify the SSH retrieval models. Figure 5.1 shows the structure of Platform Harvest and location where the experiment took place. The receiver and data recorder were setup in Jet Propulsion Laboratory (JPL) equipment shed. The antennas were deployed at the same floor and 30 meters away from the equipment shed.

A five-day experimental campaign was performed at Platform Harvest starting Aug 02, 2017. The experiment was conducted over a 72 hour period between Aug 03, 2017 and Aug 06, 2017. A total of 7.24 seconds of direct and reflected signals was collected every hour for each band (Ku,K) and each polarization. Table 5.1 is the summary of the recording parameter during the experimental campaign.

Table 5.1. Parameter of Data Recording

Parameter	Ku (12.4GHz) K (18.5GHz)	Unit
Sampling Frequency, fs	400	MHz
Sampling Quantization	8 (I & Q)	bits complex
Polarization	LHCP, RHCP	—
Recorded data length	5	sec

5.2.1 In Situ Mean Sea Level for Data Comparison

In situ SSH was acquired from a tide gauge and LiDAR system, both installed at Platform Harvest. Tide gauge values were reported every 6 minutes. Comparison SSH was found by averaging tide gauge readings from two times closest to that of the altimetry measurement. The tide gauge SSH was corrected using Significant Wave Height (SWH) to compensate for sea state effects[37]. Figure 5.5 plots the time series of in situ SSH (tide gauge), along with SWH (from buoy 46218) and wind speed (from buoy 46054). SSH varied from 0 to 1.8 meter above MSL.

The LiDAR system consisted of a downward-looking laser sensor. LiDAR mean sea level was used as a reference since measurements were collected at a rate of 50 Hz which is higher than tide gauge and were also used for generating statistics and validation of the error model. The standard deviation of LiDAR to tide gauge measurement is 2.71 cm [37].

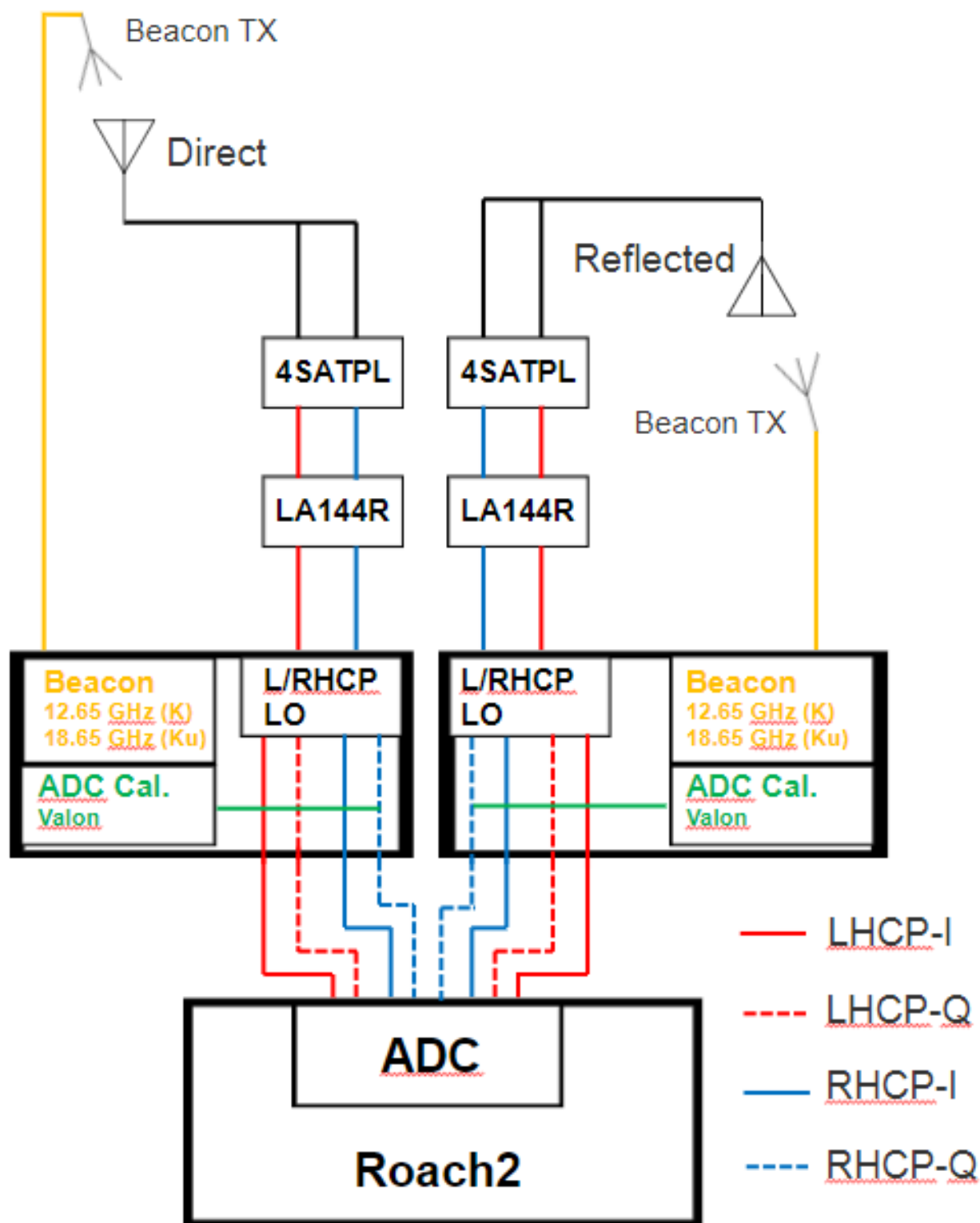


Figure 5.3. The integrated system of the Harvest experiment.

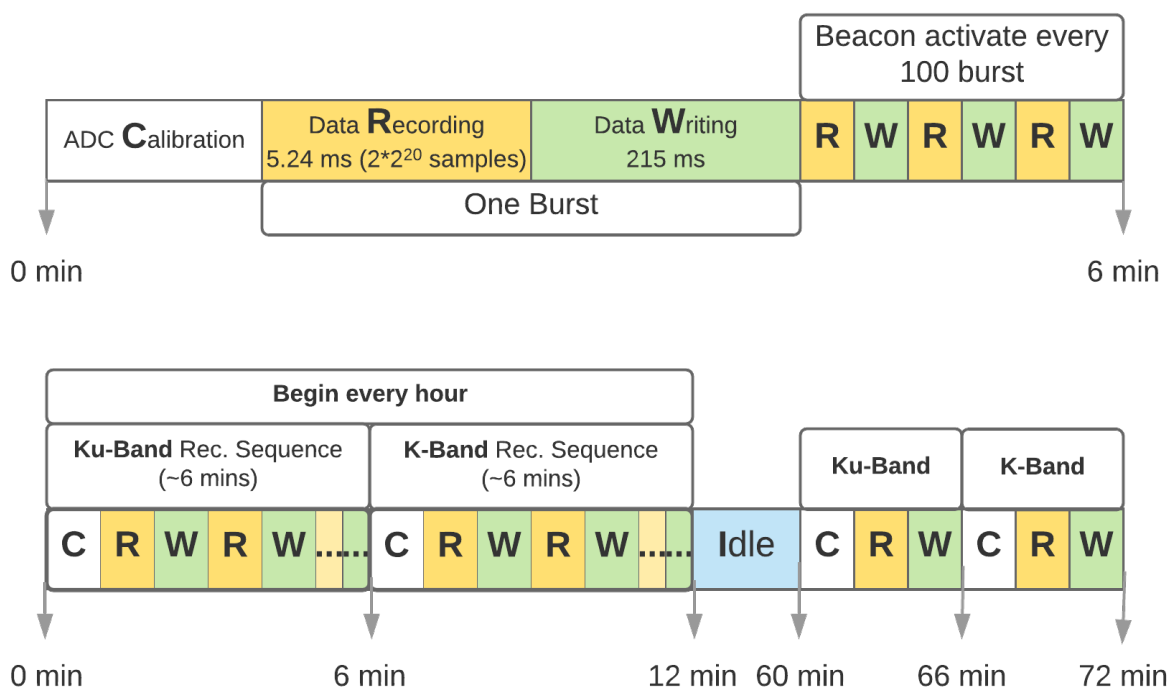


Figure 5.4. The time plan of signal recording.

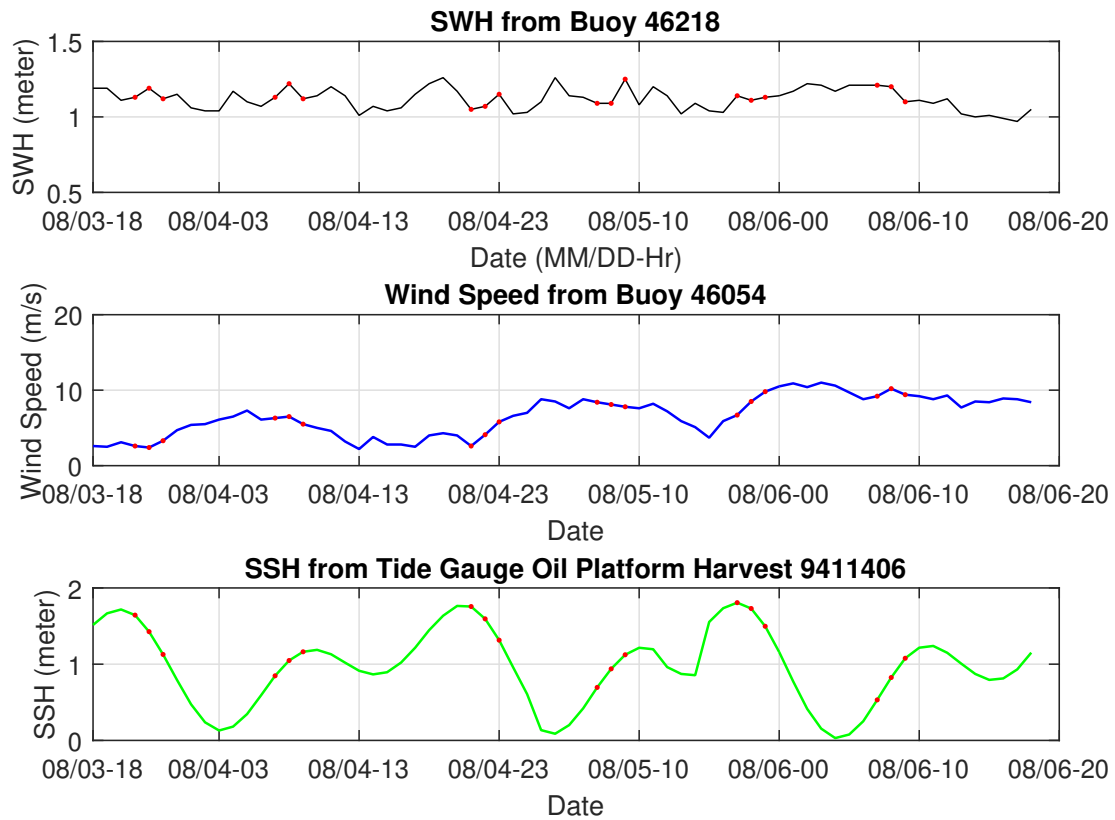


Figure 5.5. Environmental Conditions during Experiment. Red markers are the time where multiple peaks appear in RHCP data as described in results section.

6. ALTIMETRIC PRECISION MODEL EVALUATION USING KU-/K-BAND SIGNAL OF OPPORTUNITY

This chapter describes the post-processing algorithm used to evaluate Altimetric Precision Model developed in Chapter 4 using Wideband signal Ku- and K-band data collected in the experimental campaign described in Chapter 5.

6.1 Ku-/K-band Data Post-Processing

6.1.1 Data Processing

In post-processing, waveforms were computed using a coherent integration time of 4 ms (from each burst). Before cross correlating the direct and reflected signals, both ADC calibration (τ_c) and corrected frequency (f_D) were used to calibrate the time shift bias and frequency offset. The following assumptions were made for cross correlation and SSH computation: 1) The model of the signals is the same for reflected and direct signal. 2) It was assumed that the majority of the reflected power comes from a specular point reflection and the bistatic radar equation can be used to compute the reflected power.

Previously in [14], a quadratic polynomial fit ($y = ax^2 + bx + c$) was used to estimate the delay of a single channel of Ku-band signal (24 MHz) from the waveform by finding the coefficients. The same curve fitting method is applied on the wide bandwidth (400 MHz) waveforms collected in this experiment to estimate the delay. 125 waveforms (~ 27 seconds of runtime) were incoherently summed and 3 points were used to fit to the polynomial described above. The delay was obtained from the argument of the peak value of the polynomial ($-b/2a$), which corresponds to the maximum derivative. SSH was estimated from the delay using $SSH = \tau / 2 \sin(\epsilon)$. The estimated SSH was then compared with tide gauge data.

The SSH precision is also a function of SNR. The post correlation SNR was estimated from the ratio of the peak values of the post-correlation power waveforms ($I^2 + Q^2$) and the mean of the power in the noise floor.

6.1.2 Experiment Result

In this section, results of the experiment are shown to validate the error model when using total bandwidth for the LHCP transmission. Anomalous cases, at the same time, in the RHCP signal are shown to be the result of varying bandwidth and multiple peaks. We then conclude that these anomalous cases can be detected and removed from altimetry data as part of a quality control procedure.

Signal to Noise Ratio

The experimental SNR was found to be 40.5 dB for Ku-band and 36.4 dB for K-band i.e. within 0.5-1.2 dB of the predicted value from the link budget [14] introduced earlier (41.0 dB Ku-band and 37.6 dB K-band). For K-RHCP, the SNR was found to be 25.7 dB, which was lower than that for LHCP and the theoretical computation. The analysis of the cause of SNR reduction will be discussed in the following section.

Table 6.1. Link Budget Ku and K -band SoOp Altimetry from Fixed height and Orbit

Parameter	Link Budget (dB)	Experimental (dB)
KU-LHCP	41.0	40.5
KU-RHCP	41.0	41.5
K-LHCP	37.6	36.4
K-RHCP	37.6	25.7

σ_τ is the error between the estimated path delay and the SSH measurement from tide gauge for an incoherent averaging time of 5 seconds. The time history diagram of the SSH is shown in Figure 6.1 and Figure 6.2 shows a scatter plot comparing the SSH estimated from the LHCP signal in both Ku-/K-bands, after removing a fixed bias. The height biases were estimated using a linear least squares method (equivalent to the mean difference between reflected and tide gauge heights) to be 27.8 m (Ku-band) and 28.0 m (K-band). Since the antennas are mounted approximately 28.0 m above the sea surface, this estimation of height bias is reasonable. In addition, the offset of ± 0.2 m in height bias estimation between the

Ku- and K-band channels is reasonable because of the differences in cable propagation delay for two frequencies.

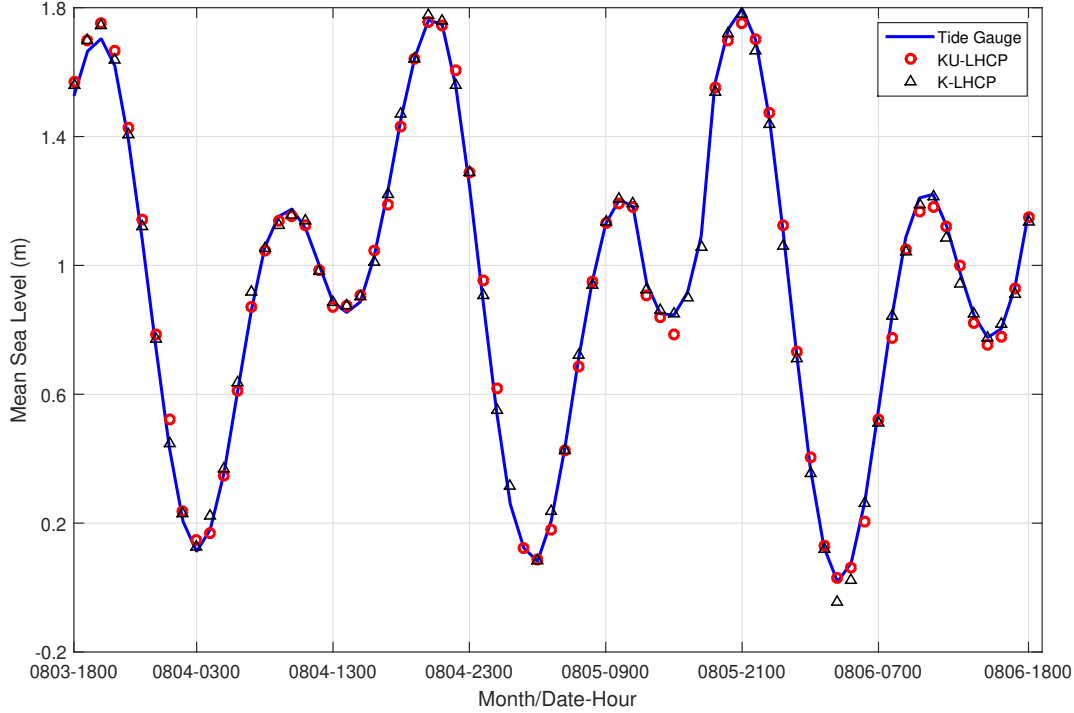


Figure 6.1. Time history of computed SSH(Ku-/K-band LHCP) after eliminating height bias vs. SSH measured by the tide gauge.

Estimated SSH was obtained after eliminating the height bias, as described above. The standard deviation was found to be 2.78 cm for Ku-band and 2.58 cm for K-band, about root mean square error 2 cm larger than the 1.52 cm computed from the error model (Eqn 4.16). Differences between the expected and computed error were found to be the result of variation in ocean condition during the 6 minute period in which the data was being recorded.

The error source from error model may be affected by the recording time not overlaying, as well as measured footprint and sea condition variation during data recording. These effects contribute about 2 cm to the total MSE. Furthermore, short integration time lengths were shown to have potential for spaceborne and airborne applications. Using a similar method, the precision estimation of spaceborne Ku- /K-Band SoOp Altimetry is shown in Table 6.2.

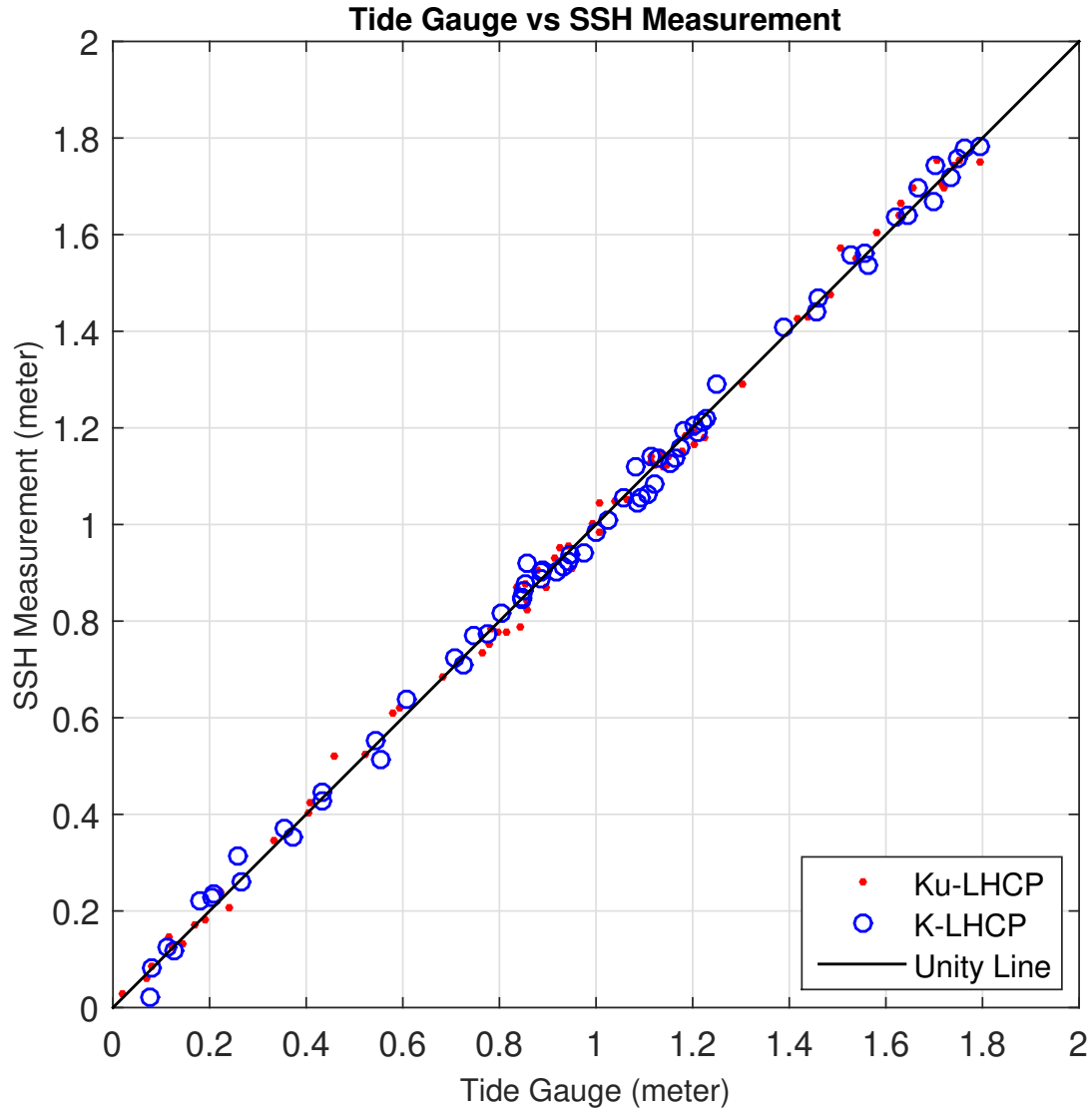


Figure 6.2. Scatter plot (Ku-/K-band LHCP) of computed SSH ($\sigma_H = 2.78$ cm) after eliminating height bias vs. SSH measured by the tide gauge.

This has been verified using LiDAR data as explained in the next subsection. Furthermore, the different and non-coincident sampling areas of the tide gauge (a point) and SoOp (an area of about $7m^2$) could also contribute to the total measurement error.

Table 6.2. The comparison of standard deviation of Ku-/K-bands between theoretical and measurement result by using tide gauge

	Theoretical (cm)	Measurement (cm)
Ku-LHCP	1.53	2.78
K-LHCP	1.51	2.58

Comparison to LiDAR

LiDAR was also used as a reference since it provides data at a higher rate than tide gauge and thus can be used to observe short term changes in the sea condition. This helped explain one of the reasons for differences between theoretical and experimental error in the previous section; variation in the SSH between tide gauge samples. Figure 6.3 shows the scatter plot comparing estimated SSH against LiDAR data for Ku-band LHCP and K-band LHCP and RHCP. Each SSH point is estimated using 0.5 seconds (125 waveforms) of incoherent averaging. The standard deviation of LiDAR tide gauge measurements is 2.71 cm [38]. It is noted that in Figure 6.3 there is no data between 11.9 m and 12.0 m. Experimental data were recorded for only a few minutes every hour. Accordingly, not every range of SSH was observed. The theoretical error in Table 6.3 is the root sum square (RSS) of the observation error 4.16) and the LiDAR variance.

Table 6.3. The comparison of standard deviation of Ku-/K-bands between theoretical and measurement result

	Theoretical (cm)	Measurement (cm)
Ku-LHCP	4.76	4.93
Ku-RHCP	4.76	9.61(5.89)
K-LHCP	4.85	4.87
K-RHCP	4.85	5.50

*Notes. 9.61 cm is the results from multiple peaks presented in Ku-RHCP, 5.89 cm is the precision that included only single peak cases.

The measured SSH standard deviation for LHCP is 0.5-1.3 cm larger than the predicted error model (incorporating the LiDAR error). The RHCP results for both Ku- and K-band have larger variances as compared to LHCP results.

Upon further inspection, multiple peaks were also found to be presented in Ku-band RHCP waveform from UTC 04:00-08:00 and 15:00-19:00 in each of the consecutive three days of the experiment (Figure 6.4). When the times exhibiting multiple peaks were not considered in the error computation, the standard deviation of Ku-RHCP decreased from 9.61 cm to 5.89 cm. The reason for appearance of multiple peaks is further explored in the next section.

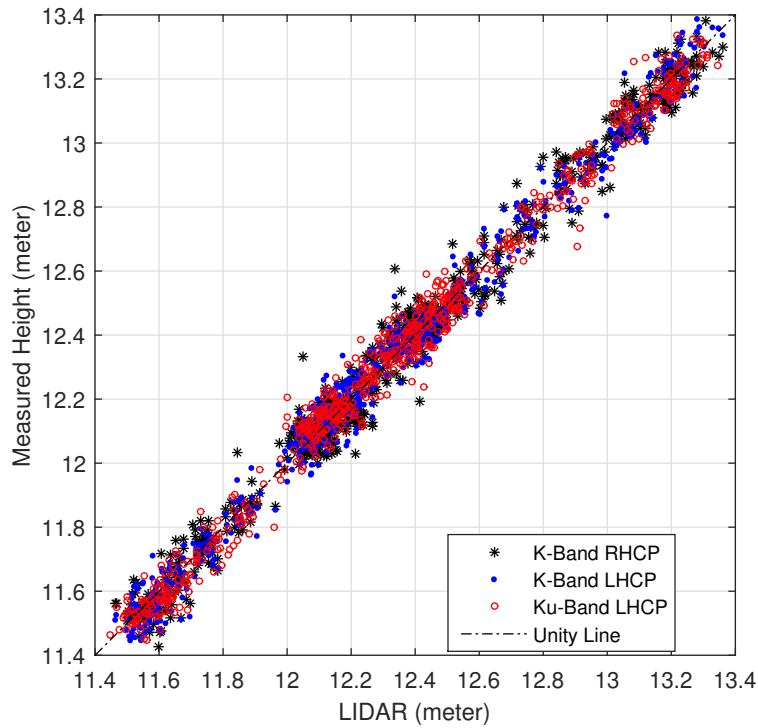


Figure 6.3. Scatter plot (Ku-LHCP) of SoOp SSH vs. Lidar SSH for Ku-band LHCP and K-band RHCP/LHCP. Statistics are given in Table 6.3.

6.1.3 Analysis - Multiple Peaks (Ku-band RHCP)

The scatter plot of Ku-RHCP (Figure 6.4) shows some instances of large bias, these were found to result from multiple peaks appearing in the cross-correlation. Additionally, the waveform time series over the experiment period (Figure 6.5) shows four features of this multiple-peak appearance: (a) It occurs at regular times each day (UTC 04:00-08:00 and

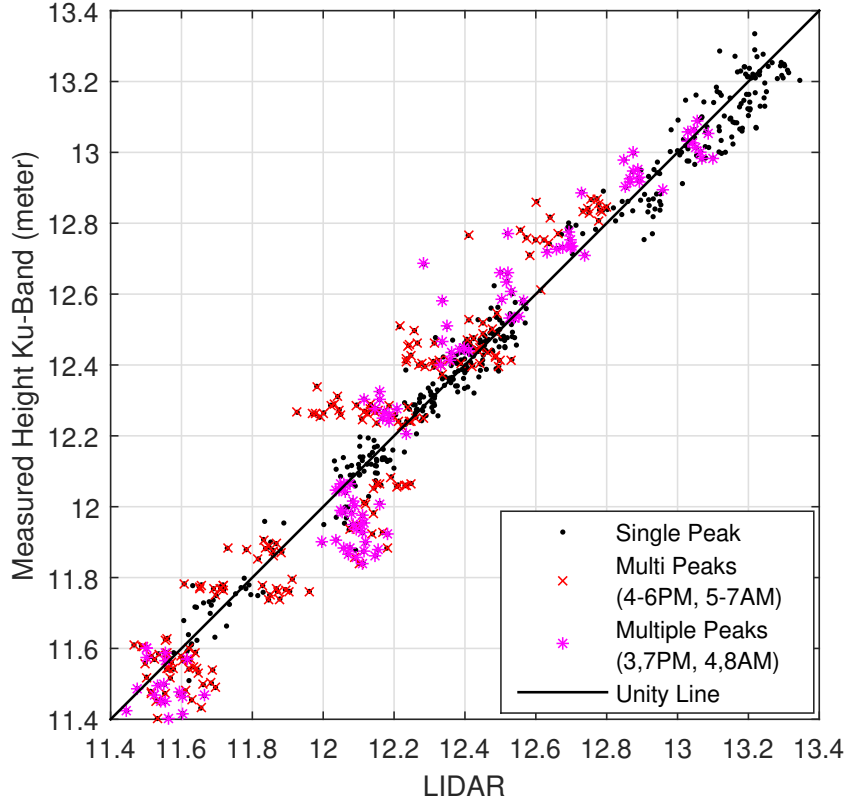


Figure 6.4. Scatter plot (Ku-band RHCP) of SoOp SSH vs. LiDAR SSH. After removing multiple peaks SSH data (marked in red and magenta), σ_H decreases to 5.89 cm

15:00-19:00), (b) It is only present in Ku-band RHCP, (c) The secondary peak appears at a lag of 4 chips (3 meter) away from main peak (d) The waveform peak power decreases as compared to the single peak instances. Given these features, we performed several tests to eliminate the possible causes of multiple peaks.

The possible causes are from multipath, multisource, L/RHCP signal leakage(LNB probe oscillator issue), sea state and transmitting source.

1. Instrument effects - Since Ku-RHCP is the only case exhibiting multiple peaks and Ku-RHCP shared the same signal path with K-RHCP in the recording system, the possibility that this effect was induced by the cable or the Front End was not considered feasible. 24-hours of data using two antennas pointed directly at the satellite and

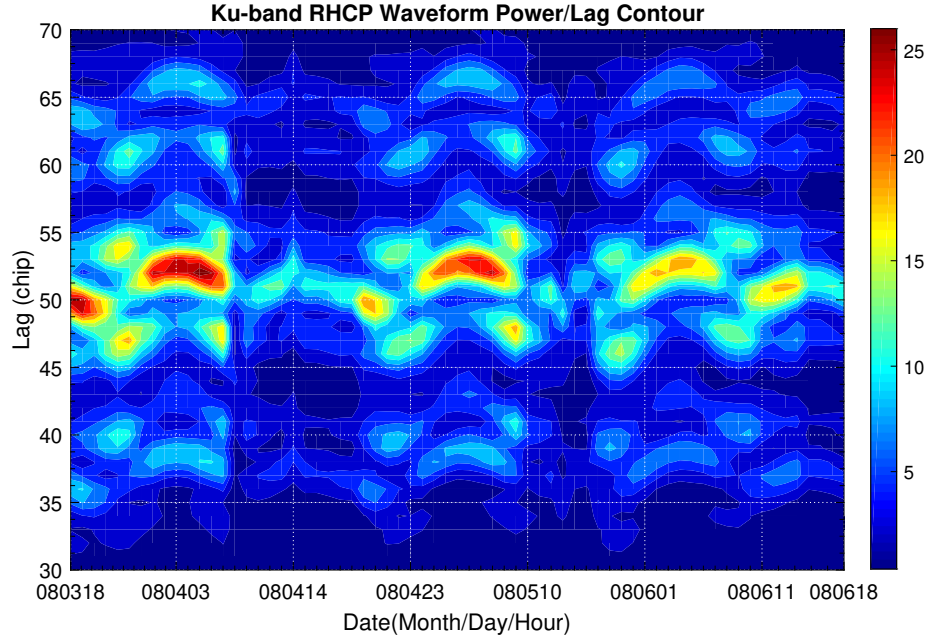


Figure 6.5. The waveform Power/Lag contour of Ku-RHCP showing effects of multipeak, x-axis: Time, y-axis: Lag(chip), Color-bar: post-correlation power waveforms $I^2 + Q^2$

- separated to have 25 m path delay in an experiment conducted in Purdue University Agronomy Center for Research and Education (ACRE, 40°28'11.9"N 86°59'30.9"W). Multiple peaks were not observed in this experiment.
2. Multipath - The antenna was facing away from the platform and since only the Ku-RHCP signal suffered from multiple peaks, the possibility of multipath reflected from infrastructure of the platform was therefore considered to be relatively low.
 3. Multisource - The orbit of every DBS adjacent to DirecTV 101°W and 99°W was modeled and the maximum path delay was found to be less than 1 meter (1 chip lag = 0.75 m), which was much less than observed multiple peaks with the measured 3 m delay.
 4. L/RHCP signal leakage - By performing cross-correlation between two polarization, a small correlation was found between these two channels. But the waveform power was found an order of magnitude less than measured same polarization waveforms for

Ku-band signals. Therefore, this was not a feasible cause. Additionally, the waveform shapes of LHCP and RHCP are different (RHCP possess side peaks but not LHCP). If the LHCP leaked to RHCP, the power level would be too low to influence the waveform, as well as the shape of the waveform would not be able to cause the observed multiple peaks.

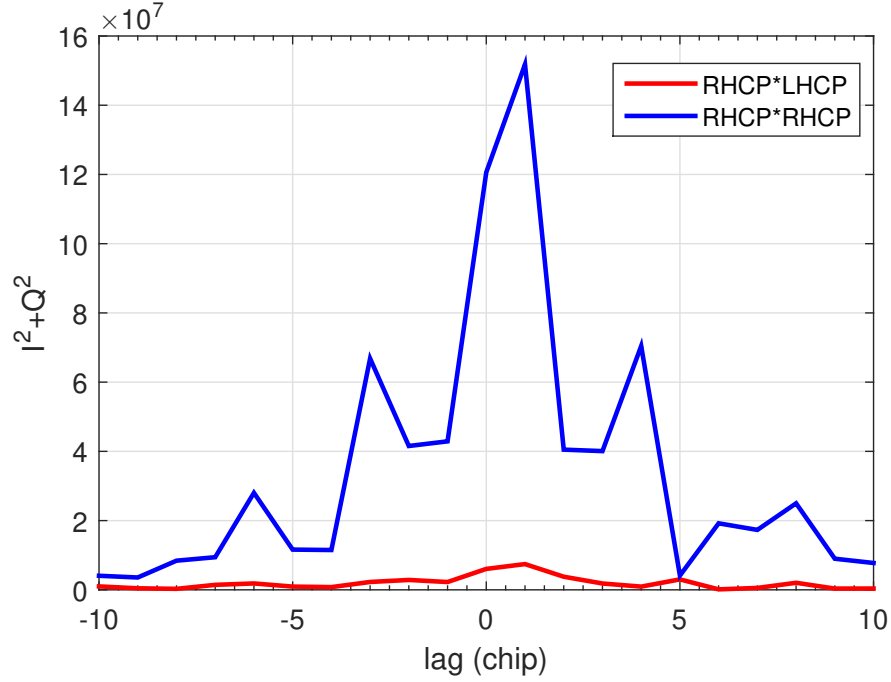


Figure 6.6. Comparison between the correlation of co-polarization (RHCP★RHCP) and cross-correlation (RHCP★LHCP)

5. Sea state - The corresponding SWH and wind speed (Red Markers in Figure 6.7) variation during experiment was not found to be correlated with the occurrence of multiple peaks. Therefore, the possibility that the multiple peaks were a result of sea state variation was found to be low.

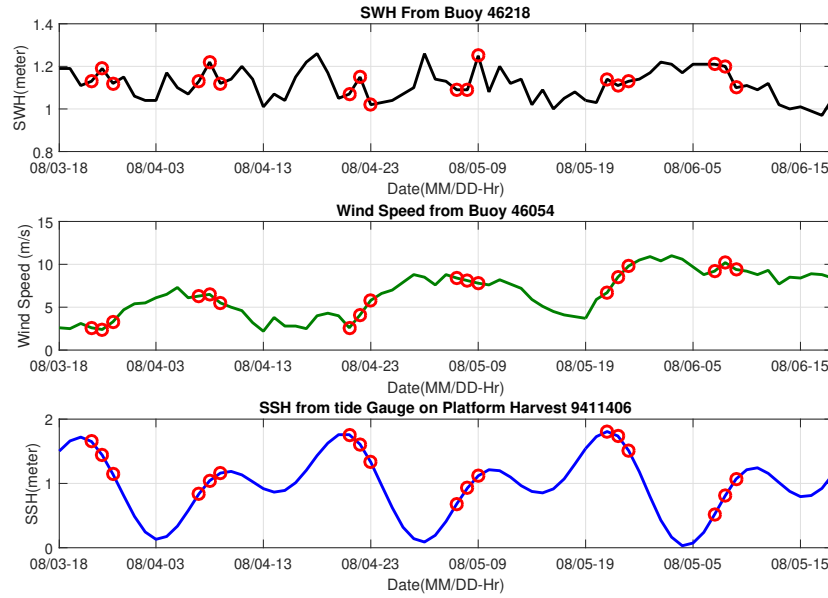


Figure 6.7. Environmental Conditions during the experiment. Red markers are the time where multiple peaks appear in RHCP data as described in results section.

6. Spot Beam - Public information from commercial website SatBeams [39] shows that Ku-band RHCP from DirecTV 4S is a spot beam. Upon further inspection, it was found that Platform Harvest is covered both by the San Francisco and Los Angeles spot beam, which may explain relatively higher power. If the overlapping spot beams were transmitting the same signal during the time when multiple peaks happened and there was a lag between these two spot beams, the resulting interference could potentially cause multiple peaks.

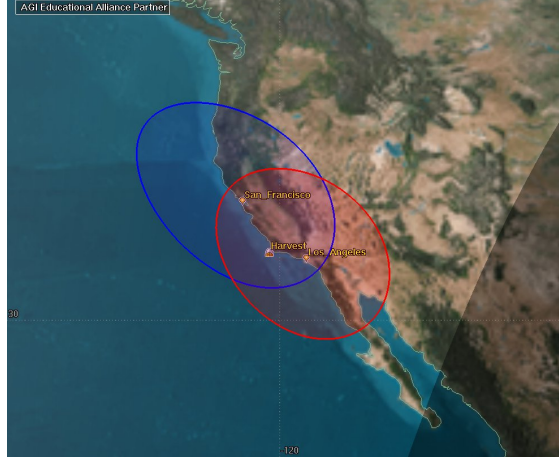


Figure 6.8. Platform Harvest under San Francisco and Los Angeles SpotBeam

6.1.4 Model Testing by Reducing Signal Bandwidth

This section is the error model testing by reducing signal bandwidth. The filter can be used to reduce the number of channels to test the error model. I reduced the channels from 2 to 10 channels in order to test the model. The power spectrum of the reduced channels is shown in Figure 6.4. The result of the standard deviation of filtered Ku-band Spectrum is shown in Table 6.4.

Table 6.4. The standard deviation of experimental data with different filter.

No. Channels	BW (MHz)	$\sigma_{SSH}(cm)$
2	50	6.23
4	100	6.12
6	150	6.08
8	200	6.24
10	250	6.19

The SSH retrieved result with a different bandwidth and the same sampling rate does not show an improvement in precision. The standard deviation of two-channel bandwidth is close to the case with more than two channels. Since the beamwidth of the telecommunication signal is narrow, the reduced bandwidth with the same sampling rate does not match the model prediction. In Figure(6.10), the slope of the 8-channel correlation power waveform is

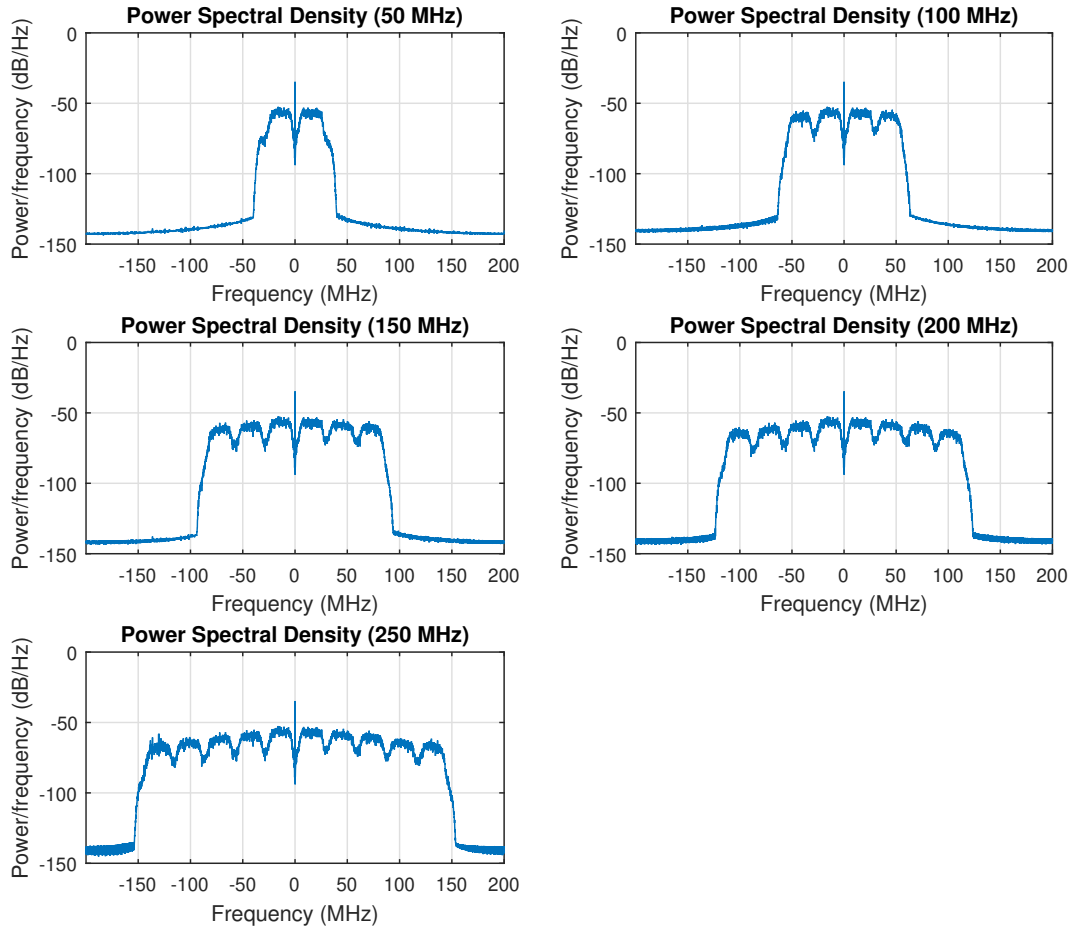


Figure 6.9. The Power Spectrum Density of different filter. The result of the experiment data of different filter is shown in Table(6.4)

steeper than the power waveform of 2-channel. Increasing the signal bandwidth does change the gradient of the power waveform.

The precision of different effective bandwidths of the signal is evaluated in this section. This method uses the signal bandwidth we collected from Harvest and the effective bandwidth is reduced by downsampling the signal time series data by using interpolation. The interpolation method that I used in the downsampling is linear. The downsampling bandwidth of KU-LHCP is shown in Figure 6.12.

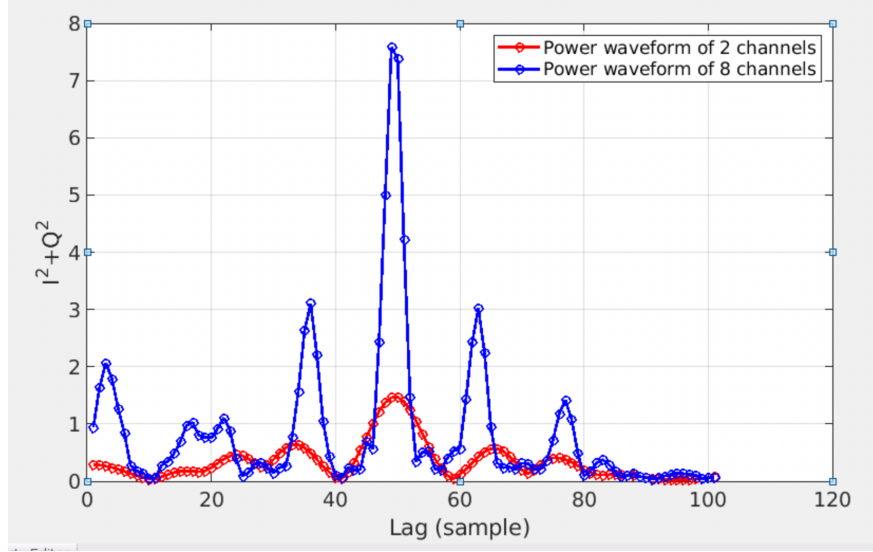


Figure 6.10. The power waveform of 2 channels and 8 channels filtering. The slope of the 8 channels wideband signal is steeper than power waveform of 2 channels.)

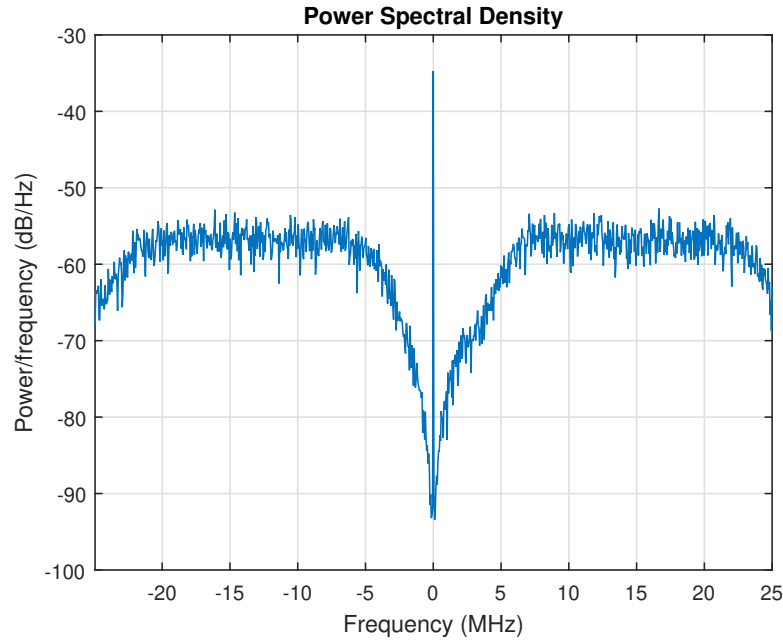


Figure 6.11. The spectrum by using resample function with 50 MHz (2 channels)

According to the previous section, the reduced bandwidth with the same sampling rate does not reduce the precision of the SSH prediction. This section evaluates the precision of

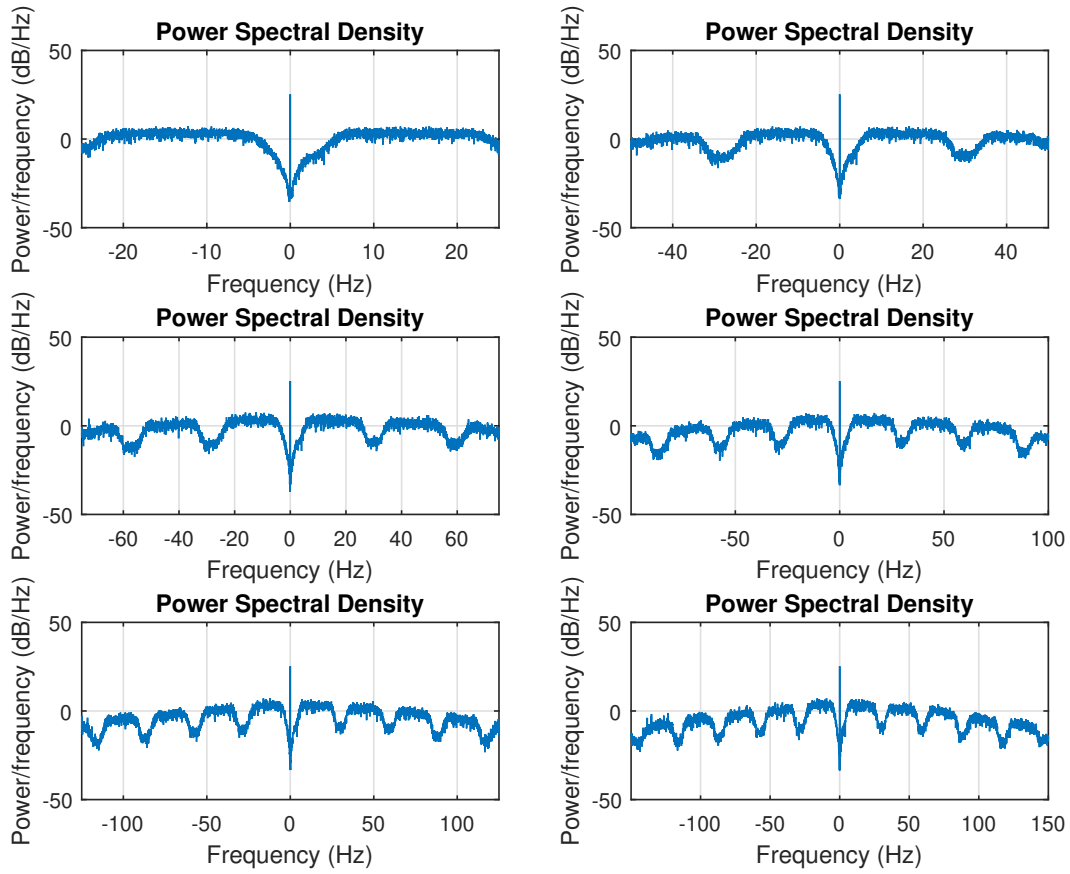


Figure 6.12. The Power Spectrum Density of different Bandwidth. The downsampling is using linear interpolation of the time series data we collect from the experiment.

the SSH of data linear downsampling to 50-240 MHz and compared the precision with error model prediction. The result of the different bandwidth testing is shown in Table 6.5

Table 6.5. The standard deviation of experimental data with different bandwidth.

Bandwidth	σ_{model} (cm)	$\sigma_{exp}(cm)$
50	38.14	31.53
100	19.23	20.47
150	12.73	11.97
200	9.54	10.47
240	7.95	8.12

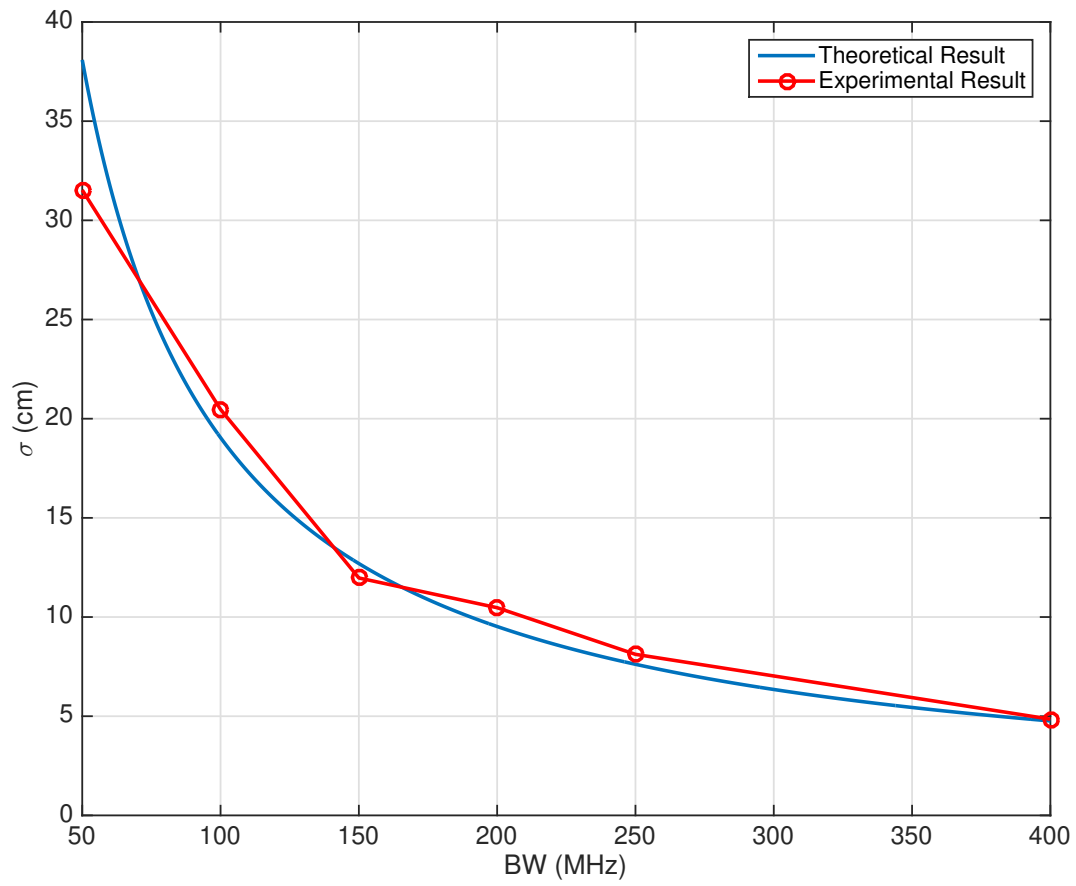


Figure 6.13. This graph shows the theoretical estimated precision and the experimental data

From the result of reducing bandwidth, the prediction meets the result of the measurement.

7. ALTIMETRY PRECISION MODEL EVALUATION

This section uses the wideband signal data to evaluate the result from the CRLB method. The first subsection shows the Equivalent Noise Bandwidth in the model and evaluates the precision using ENBW in the error model estimation. The next section compares the estimated precision from the full bandwidth and CRLB method with the experimental data. Lastly, the evaluation of these methods will be discussed.

7.1 Equivalent Noise Bandwidth

This model used the Equivalent Noise Bandwidth as an effective bandwidth, B , in Eqn.(4.16). The first method is using the peak power of the spectrum to compute the ENBW. The second approach is using the average power of the center channels as the maximum value of the spectrum to compute the ENBW. The third approach is computing the ENBW channel by channel. The ENBW computed by first and second methods is shown in Figure 7.1. In Table 7.1, the ENBW of different approaches is shown. Since the average spectrum is still too noisy to use the maximum value of the spectrum, the ENBW of the first method is lower than expected. From the spectrum, the power of the center channels is stronger than the outerbounds, which is not what the spectrum is shown on the spectrum analyzer (Figure 2.1, 2.2). The alternative way to compute the ENBW for the error model is computing the ENBW of each channel and sum the ENBW of each channel as the effective bandwidth to the error model (Eqn 4.16). From the result in Table 7.1, the method using the sum of ENBW of each channel is more reasonable compare to other methods.

Table 7.1. This table is the comparison of different method approach to compute the ENBW.

Method	ENBW(MHz)
Maximum power of the PSD	82
Mean power of the center channel	151
Sum of ENBW of each channel	312

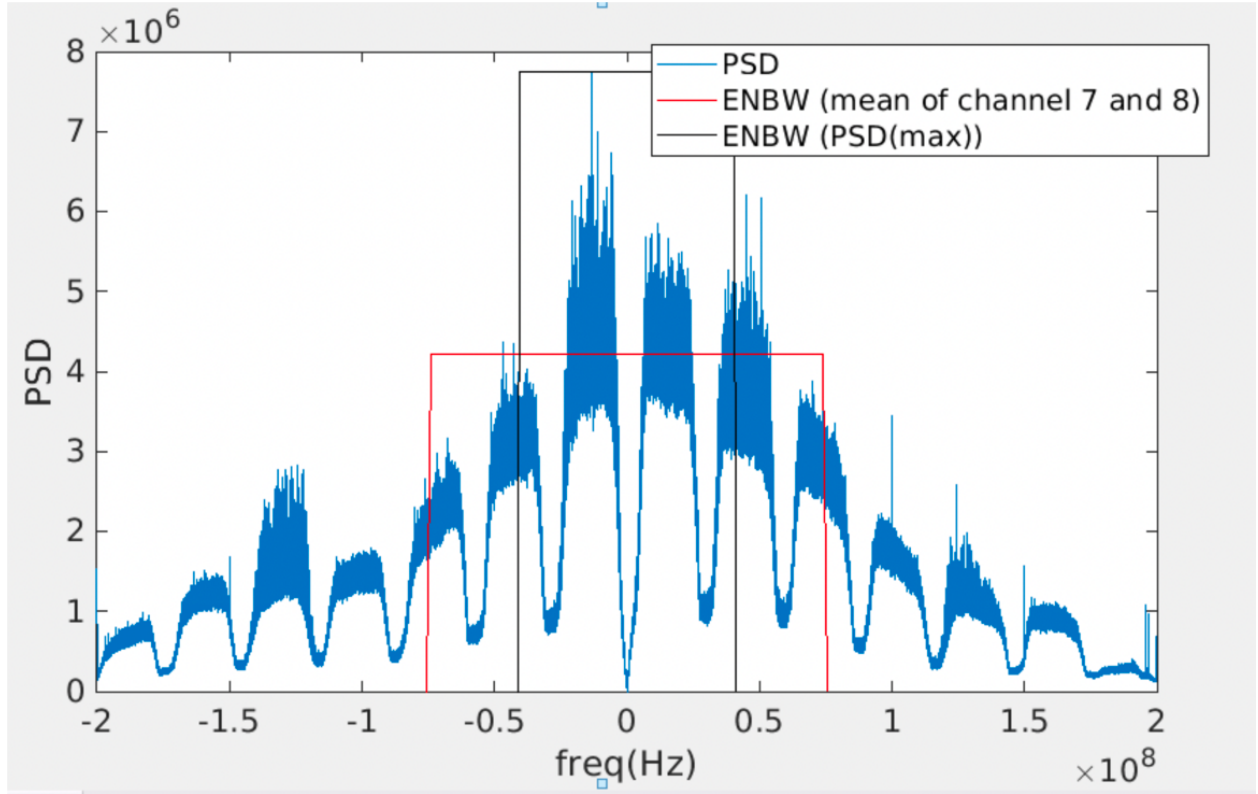


Figure 7.1. The Ku-LHCP spectrum and its ENBW.

7.2 Cramer Rao Lower Bound

This section evaluates the estimated precision of different CRLB model approaches and the experimental result.

CRLB (Sample Independent)

When the waveform is independent, the mean peak power waveform and the local gradient can be used to compute the standard deviation of the path delay. The example of the measured mean power waveform is shown in Figure 7.2.

RMS/Gabor Bandwidth

The power spectrum of the cross-correlation waveform can compute the RMS bandwidth (second moment). In Figure 7.3, two spikes occurred at 150 MHz. These spikes are due

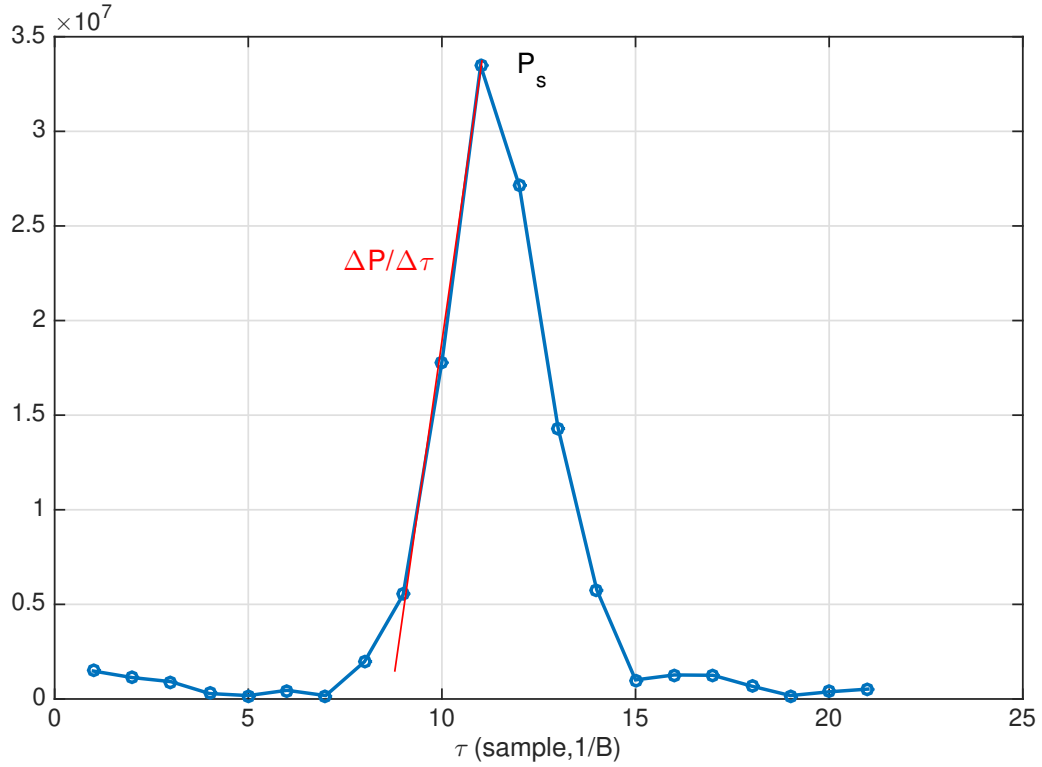


Figure 7.2. The example of the measured correlation waveform and the parameters to estimate the precision.

to the calibrated signal from the beacon mounted on the antenna. Before computing RMS bandwidth, these spikes have to be removed since the magnitude of the second moment of these spikes will cause the estimation error (Figure 7.4).

7.2.1 Model Performance and Result

The predicted precision from the CRLB method of both Ku-LHCP, K-LHCP, and K-RHCP are shown in Table 7.2. Since we considered three points least square estimator to compute the estimated delay, the ratio of the power and the slope of the leading edge can be expressed as $1/B$. The prediction by using an independent sample of the waveform did not perform well compared to another approach. The result implied that using the mean waveform power and the local gradient can not effectively predict the path delay precision estimation when the waveform sample is not independent.

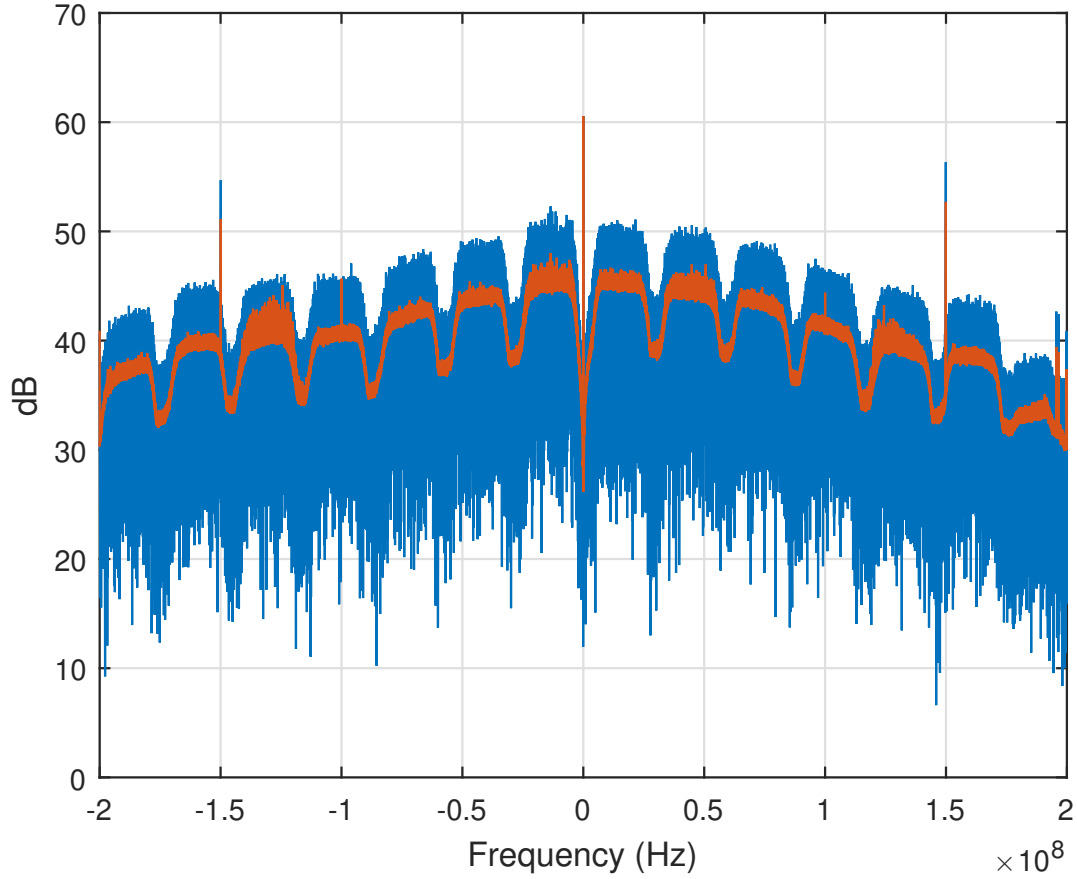


Figure 7.3. The measured Ku-Band spectrum, the blue spectrum is single 4ms integration spectrum, the orange spectrum is the average of 1 sec of the measured spectrum.

For LHCP cases, the estimated standard deviation from Full Bandwidth, ENBW, and the CRLB model works well with the experimental result. From section 6.1.2, K-RHCP suffered a reduction of the SNR, and the precision is lower than the models' prediction. The Full Bandwidth and ENBW model are insensitive to the anomaly measurement. In the second column of Table 7.2, the CRLB method still can not accurately predict the precision of the SNR reduction case from K-RHCP.

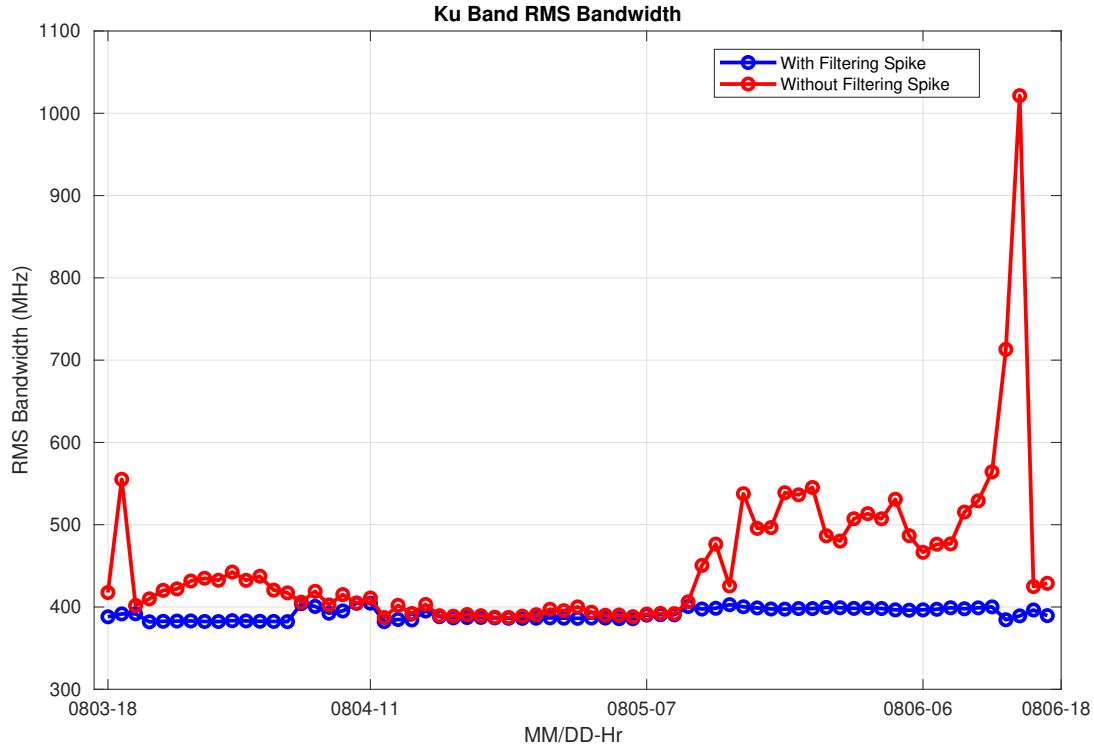


Figure 7.4. The RMS bandwidth with/without beacon spike removal.

Table 7.2. This table is the comparison of different model approach.

Model	KU-LHCP	K-RHCP	K-LHCP
Full Bandwidth (400MHz)	4.76	4.85	4.85
ENBW	6.10	5.76	5.69
CRLB (Sample Indep)	13.11	16.86	13.98
RMS Bandwidth	5.55	5.01	4.91
General CRLB	5.24	4.60	4.69
Experiment	4.93	5.64	4.97

7.3 Time Series K-Band RHCP Evaluation

This section evaluates the K-band RHCP result in time series. First, the root mean square bandwidth (Eqn(4.34)) of K-RHCP in time series are shown in Figure 7.5. In Figure 7.5, the RMS bandwidth is not consistent like LHCP (Figure 7.4), but changes each different time region. In this case, I categorized the measurement into five different regions (Figure 7.6).

The shape of the normalized signal spectrum varies over different regions. The computed RMS bandwidth and SNR of each section are shown in table 7.3.

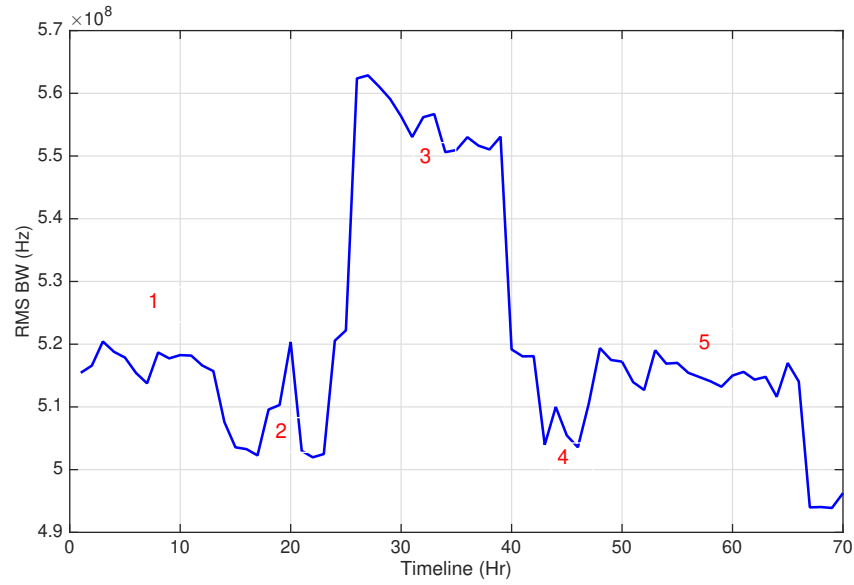


Figure 7.5. The RMS bandwidth of K-RHCP over recording time.

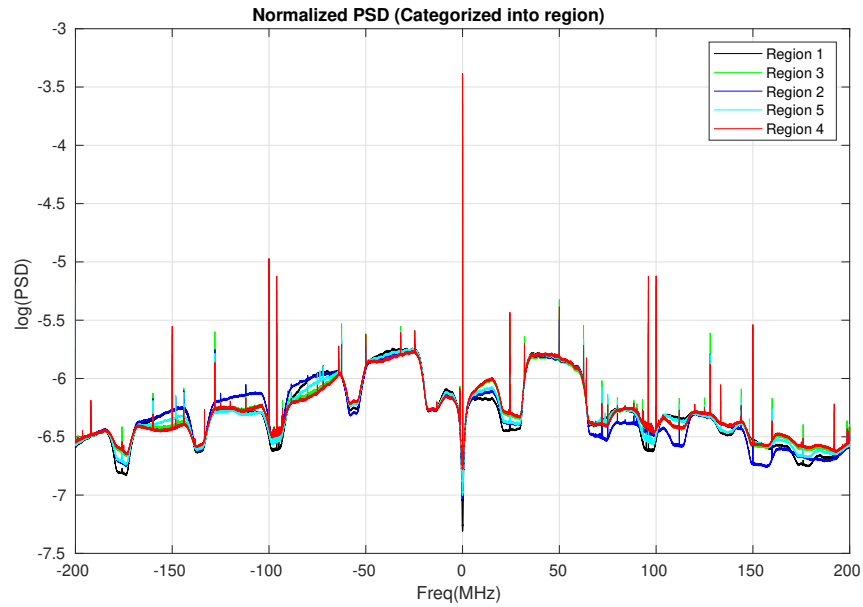


Figure 7.6. The normalized signal spectrum of K-RHCP of different region, divided into 5 periods

Table 7.3. The RMS bandwidth and SNR of different section.

Section	RMS BW (MHz)	SNR (dB)
1	82	26.21
2	81	24.52
3	88	26.42
4	81	23.32
5	81	23.40

Table 7.4. This table is the comparison of different model approach by different region of time.

	R1	R2	R3	R4	R5
Full Bandwidth	4.85	4.85	4.85	4.85	4.85
ENBW	5.73	5.59	5.83	5.70	5.57
RMS BW	5.00	4.99	4.67	4.84	4.99
General CRLB	4.91	4.78	4.21	4.62	4.52
Experiment	5.49	7.47	6.47	5.13	4.25

The computed RMS bandwidths are different for each section of the measurement. In Table 7.4, the experiment result shows that regions 2 and 3 are the worst in precision compared to the model prediction. Besides, all models can not effectively predict the anomaly region. In Table 7.3, the SNR of the different sectors shows no significant reduction, the increase of measurement error is not due to the SNR factor, and the model is not able to detect the precision reduction for regions 2 and 3. In Figure 7.7, both experimental precision and RMS bandwidth are shown. The result shows that the experimental data has a larger error when the RMS bandwidth is increasing/decreasing. The precision, which is highlighted in Figure 7.7, is the measurement where the transition occurred. The hypothesis is the precision of measurement reduces during the transition period. In Table 7.5, the measured data recorded from the transition period are removed, and the comparison result is shown below,

After taking the measured data as an outlier during the transition time, the Full bandwidth (400MHz) model can predict the precision of three different measurement cases.

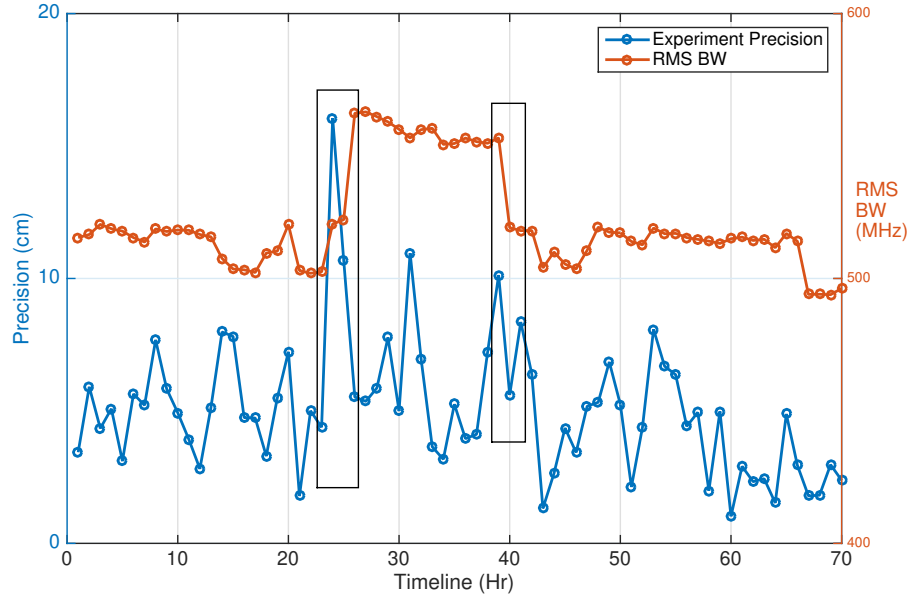


Figure 7.7. The RMS bandwidth vs Experiment Precision of K-RHCP over recording time.

Table 7.5. This table is the comparison of different model approach. The data on the transition period are moved for K-RHCP measurement.

Model	KU-LHCP	K-RHCP	K-LHCP
Full Bandwidth (400MHz)	4.76	4.85	4.85
ENBW	5.62	5.65	5.63
CRLB (Sample Indep)	13.11	16.86	13.98
RMS Bandwidth	5.55	5.01	4.91
General CRLB	5.24	4.60	4.69
Experiment	4.93	4.96	4.97

From Figure 7.8, the precision estimation from the general gaussian CRLB model is the highest, which is acting as a lower bound of the path delay estimation. The Full Bandwidth model can work well to predict the precision of the path delay estimation when the data measured during the transmitted spectrum is not in the transition period.

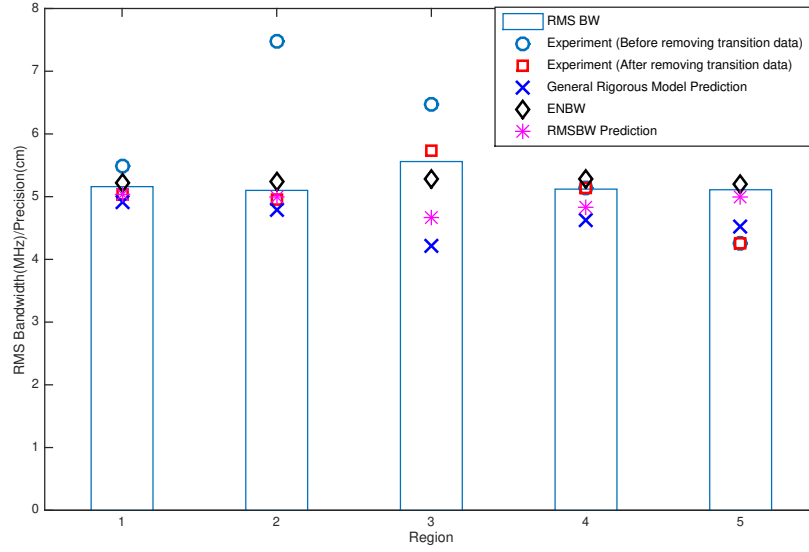


Figure 7.8. The comparison between model prediction and measured precision of K-RHCP over region by region.

7.3.1 Comparison between Model of Measured Data in Time Series.

Previously, model prediction divided into 5 periods of K-Band RHCP cannot predict the anomaly case of the K-RHCP measurement. The experimental result will compare to the model prediction in time series to determine whether the model can predict the anomaly.

KU-LHCP

This section is the time series comparison between experimental results and the CRLB model approach. In Figure 7.9,7.11,7.13, the RMS bandwidth can not track the change of the precision. Figure 7.10, 7.12, 7.14 are the model prediction using general CRLB method. The general CRLB is not only acting as the lower bound of the path delay estimation, but it is also better in showing the precision variation during time series comparison.

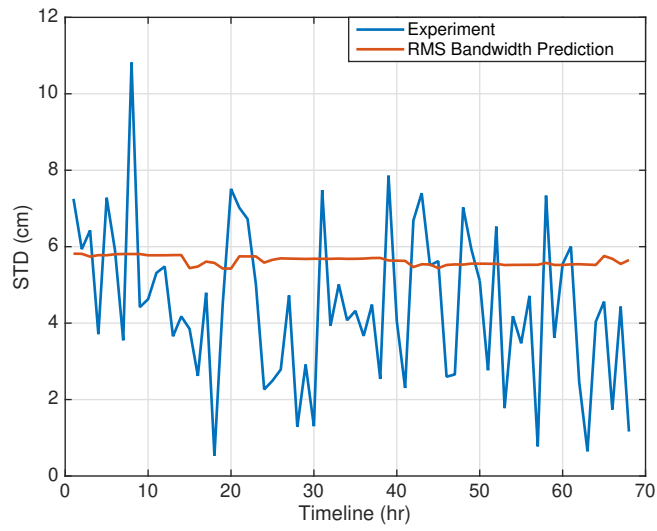


Figure 7.9. The RMS bandwidth model prediction vs Experiment Precision of KU-LHCP over recording time.

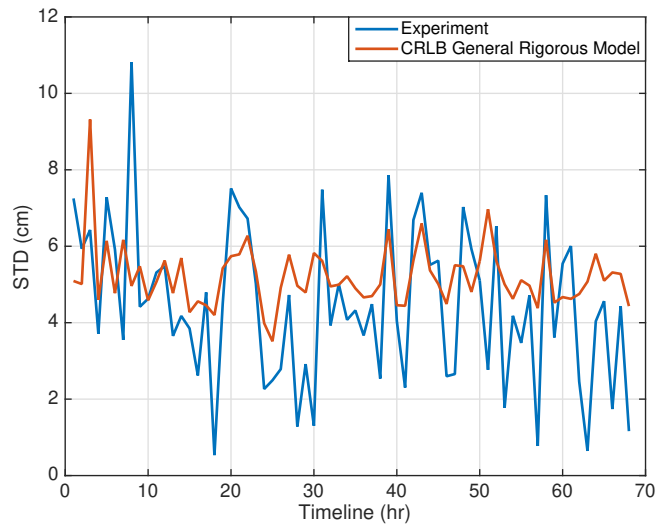


Figure 7.10. The General CRLB model prediction vs Experiment Precision of KU-LHCP over recording time.

K-LHCP

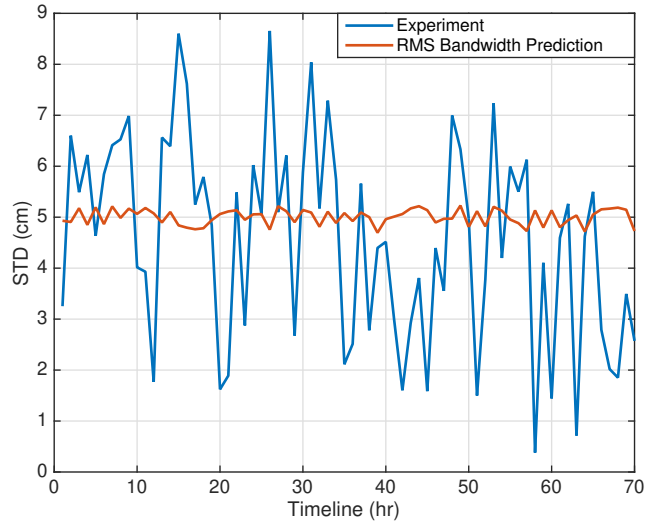


Figure 7.11. The RMS bandwidth model prediction vs Experiment Precision of K-LHCP over recording time.

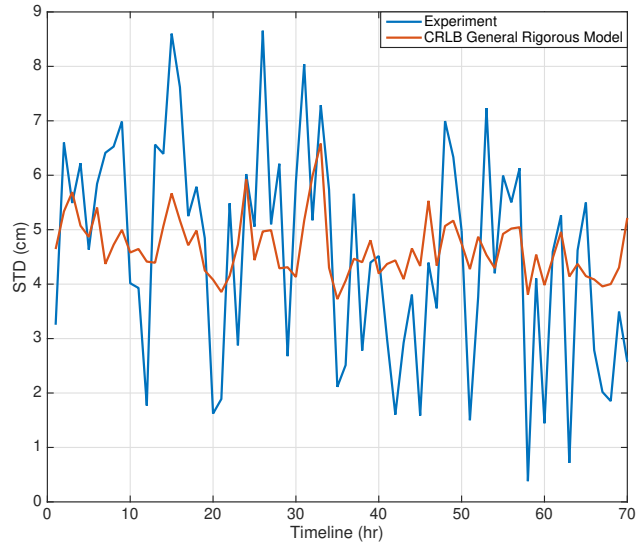


Figure 7.12. The General CRLB model prediction vs Experiment Precision of K-LHCP over recording time.

K-RHCP

7.4 Summary

This chapter compares the different model approach with the experimental result. In LHCP measurement, the Full Bandwidth model can predict the precision of the path delay

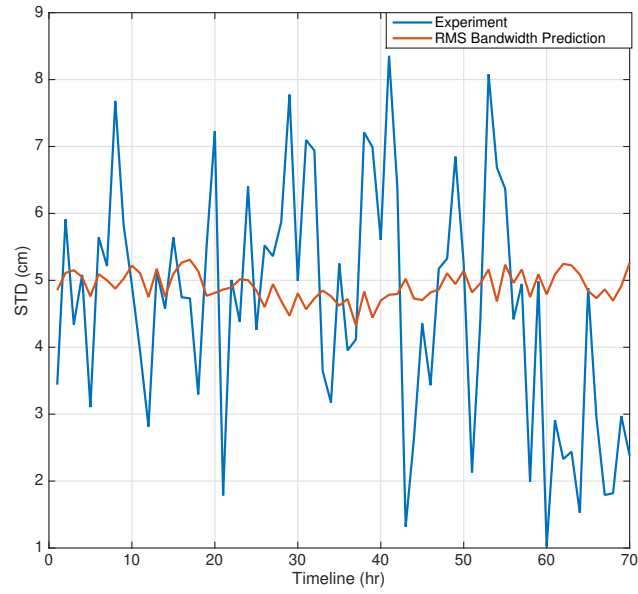


Figure 7.13. The RMS bandwidth model prediction vs Experiment Precision of K-RHCP over recording time.

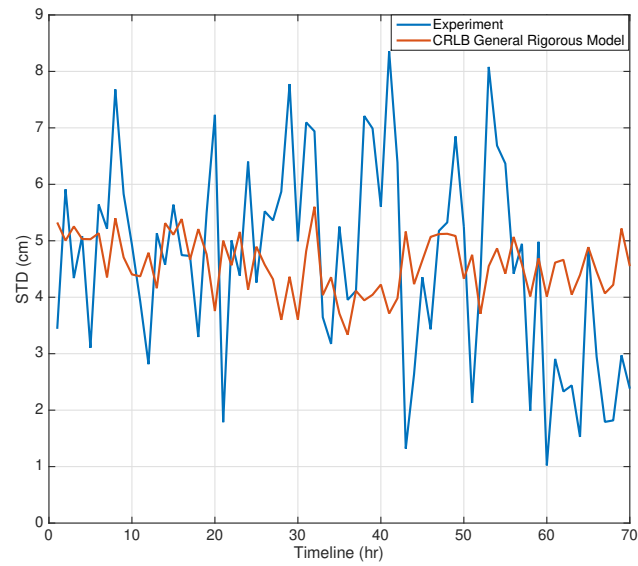


Figure 7.14. The General CRLB model prediction vs Experiment Precision of K-RHCP over recording time.

measurement in most of the cases. For the anomaly K-RHCP case, although all the models can not predict the accuracy, after excluding the measurement data during the transition period, the Full Bandwidth can work well in the K-RHCP measurement.

In K-RHCP measurement, the RMS bandwidth shows that the transmitted signal was changing during the experiment. The measurement had a higher error when the RMS bandwidth was increasing/decreasing from one state to another.

The general gaussian CRLB model prediction is acting as a lower bound of the precision of the measurement. Also, the general Gaussian CRLB model can provide partial trend information of the precision in the measurement.

8. CONCLUSION

To show the feasibility of altimetry (SSH estimation) from SoOp utilizing the full transmitted bandwidth consisting of multiple data channels, an experimental campaign was deployed on Platform Harvest. Both polarization (LHCP and RHCP) are recorded during the experiment. Although the RHCP signal had multiple peaks and power drop issues during a certain period, the LHCP's results show that this approach has the potential of using multiple channels as a wideband signal for SSH retrieval. The results from the LHCP signal validate the error model as well as the hypothesis that the Full Bandwidth can be processed as one channel.

Two anomalous cases were observed, in the K-band and Ku-band RHCP transmissions. First, multiple peaks appeared at regular time intervals in the Ku-band RHCP waveforms. Although there is no definitive conclusion as to the cause of this phenomenon, it was noted that the experiment location was within the footprint of two spot-beams. The second anomalous was the reduction of SNR in the K-band RHCP transmission, determined to be the result of the disappearance of one of the data channels. When the error model was applied only to the periods exhibiting single peaks (for K-RHCP) or with substitution of an effective bandwidth spanning the actual transmitting channels, good agreement was found between the experiment and theory.

Since there were anomalous cases (RHCP), which induced the reduction of measurement precision, an alternative precision estimation approach, Cramer Rao Lower Bound, was introduced to determine if the anomaly measurement can be detected. From the derivative result, there are three different estimation approaches, 1. CRLB sample independent, 2. RMS Bandwidth, 3. General CRLB (covariance). From the results of model prediction, these estimation approaches can not predict the anomalous case. However, the RMS bandwidth of the measured signal spectrum of K-RHCP showed the transmitted spectrum change. The precision of the measurement was reduced during the transition period. When the measurement data from the transition period was removed, the Full bandwidth model result would match the experiment result. The general Gaussian CRLB does not only act as a lower bound, but it can also provide the information of changing trends of the measurement precision. Both types of anomalies were easy to detect, suggesting that a necessary ground

support component of a SoOp altimetry mission would be a capability of monitoring the transmitted signal properties for quality control, allowing corrupted measurements to be removed and the data covariance to be adjusted.

Future work would include the further investigation of the multiple peaks and SNR reduction (signal spectrum change) issue by extending the measurement time duration of the anomaly period. In addition, the precision orbit determination of the Geostationary Communications Satellite by using wideband signal will be the next step to reduce altimetry error.

REFERENCES

- [1] L.-L. Fu, D. B. Chelton, P.-Y. Le Traon, and R. Morrow, “Eddy dynamics from satellite altimetry,” *Oceanography*, vol. 23, no. 4, pp. 14–25, 2010.
- [2] L.-L. Fu and A. Cazenave, *Satellite altimetry and earth sciences: a handbook of techniques and applications*. Academic Press, 2000, vol. 69.
- [3] R. Morrow and P.-Y. Le Traon, “Recent advances in observing mesoscale ocean dynamics with satellite altimetry,” *Advances in Space Research*, vol. 50, no. 8, pp. 1062–1076, 2012.
- [4] J. C. McWilliams, “Submesoscale currents in the ocean,” in *Proc. R. Soc. A*, The Royal Society, vol. 472, 2016, p. 20160117.
- [5] L. L. Fu, E. J. Christensen, C. A. Yamarone, M. Lefebvre, Y. Menard, M. Dorrer, and P. Escudier, “TOPEX/POSEIDON mission overview,” *Journal of Geophysical Research: Oceans (1978–2012)*, 99(C12):24369–24381, 2009. DOI: [10.1080/01490419.2011.590114](https://doi.org/10.1080/01490419.2011.590114).
- [6] T. H. Durrant, D. J. Greenslade, and I. Simmonds., “Validation of Jason-1 and Envisat Remotely Sensed Wave Heights,” *Journal of Atmospheric and Oceanic Technology*, 26(1):123–134, 1994. DOI: [10.1080/01490419.2011.590114](https://doi.org/10.1080/01490419.2011.590114).
- [7] J. Lambin, R. Morrow, L. L. Fu, J. K. Willis, H. Bonekamp, J. Lillibridge, J. Perbos, G. Zaouche, P. Vaze, and e. a. Walid Bannoura, “The OSTM/Jason-2 mission,” *Marine Geodesy*, 33(S1):4–25, 2010. DOI: [10.1080/01490419.2011.590114](https://doi.org/10.1080/01490419.2011.590114).
- [8] T. Chronis, V. Papadopoulos, and E. Nikolopoulos., “QuickSCAT observations of extreme wind events over the Mediterranean and Black Seas during 2000–2008.,” *International Journal of Climatology*, 31(14):2068–2077, 2011. DOI: [10.1080/01490419.2011.590114](https://doi.org/10.1080/01490419.2011.590114).
- [9] M. Martin-Neira, “A Passive Reflectometry and Interferometry System (PARIS)- Application to Ocean Altimetry,” *ESA journal*, vol. 17, no. 4, pp. 331–355, 1993.
- [10] S. T. Lowe, C. Zuffada, Y. Chao, P. Kroger, L. E. Young, and J. L. LaBrecque, “5-cm-Precision aircraft ocean altimetry using GPS reflections,” *Geophysical Research Letters*, vol. 29, no. 10, 2002.
- [11] H. Carreno-Luengo, H. Park, A. Camps, F. Fabra, and A. Rius, “GNSS-R Derived Centimetric Sea Topography: An Airborne Experiment Demonstration,” *Journal of Selected Topics in Applied Earth Observations and Remote Sensing, IEEE*, vol. 6, no. 3, pp. 1468–1478, 2013.

- [12] R. Shah, J. L. Garrison, and M. S. Grant, "Demonstration of Bistatic Radar for Ocean Remote Sensing Using Communication Satellite Signals," *Geoscience and Remote Sensing Letters, IEEE*, vol. 9, no. 4, pp. 619–623, 2012.
- [13] S. Ribo, J. C. Arco, S. Oliveras, E. Cardellach, A. Rius, and C. Buck, "Experimental results of an X-Band PARIS receiver using digital satellite TV opportunity signals scattered on the sea surface," *IEEE Transactions on Geoscience and Remote Sensing*, vol. 52, no. 9, pp. 5704–5711, 2014.
- [14] R. Shah and J. L. Garrison, "Precision of Ku-Band Reflected Signals of Opportunity Altimetry," *IEEE Geoscience and Remote Sensing Letters*, vol. 14, no. 10, pp. 1840–1844, 2017, ISSN: 1545-598X. DOI: [10.1109/LGRS.2017.2737949](https://doi.org/10.1109/LGRS.2017.2737949).
- [15] M. McPhaden., "Evolution of the 2006–2007 El Niño: The Role of Intraseasonal to Interannual Time Scale Dynamics," *Advances in Geosciences*, 14(14):219–230, 2008. DOI: [10.1080/01490419.2011.590114](https://doi.org/10.1080/01490419.2011.590114).
- [16] NASA, "Responding to the Challenge of Climate and Environmental Change: NASA's Plan for a Climate-Centric Architecture for Earth Observations and Applications from Space.," <http://science.nasa.gov/media/medialibrary/2010/07/01/Climate-Architecture-Final.pdf>, 2010. DOI: [10.1080/01490419.2011.590114](https://doi.org/10.1080/01490419.2011.590114).
- [17] J. A. Church, N. J. White, C. M. Domingues, D. P. Monselesan, and E. R. Miles, "Chapter 27 - sea-level and ocean heat-content change," in *Ocean Circulation and Climate*, ser. International Geophysics, G. Siedler, S. M. Griffies, J. Gould, and J. A. Church, Eds., vol. 103, Academic Press, 2013, pp. 697–725. DOI: <https://doi.org/10.1016/B978-0-12-391851-2.00027-1>. [Online]. Available: <https://www.sciencedirect.com/science/article/pii/B9780123918512000271>.
- [18] R. Cheney, "Satellite altimetry," in *Encyclopedia of Ocean Sciences*, J. H. Steele, Ed., Oxford: Academic Press, 2001, pp. 2504–2510, ISBN: 978-0-12-227430-5. DOI: <https://doi.org/10.1006/rwos.2001.0340>. [Online]. Available: <https://www.sciencedirect.com/science/article/pii/B012227430X003408>.
- [19] L. H. Holthuijsen, "Waves in Oceanic and Coastal Waters.," *Cambridge University Press*, 2007.
- [20] J. L. Garrison, S. J. Katzberg, and M. I. Hill., "Effect of sea roughness on bistatically scattered range coded signals from the global positioning system.," *Geophysical Research Letters*, 25(13):2257–2260, 1998.
- [21] V. U. Zavorotny and A. G. Voronovich, "Scattering of GPS Signals from the Ocean with Wind Remote Sensing Application," *Geoscience and Remote Sensing, IEEE Transactions on*, vol. 38, no. 2, pp. 951–964, 2000.

- [22] E. Cardellach, F. Fabra, O. Nogués-Correig, S. Oliveras, S. Ribó, and A. Rius, “GNSS-R ground-based and airborne campaigns for ocean, land, ice, and snow techniques: Application to the GOLD-RTR data sets,” *Radio Science*, vol. 46, no. 6, 2011.
- [23] J. L. Garrison, A. Komjathy, V. U. Zavorotny, and S. J. Katzberg, “Wind Speed Measurement Using Forward Scattered GPS Signals,” *Geoscience and Remote Sensing, IEEE Transactions on*, vol. 40, no. 1, pp. 50–65, 2002.
- [24] M. Martín-Neira, M. Caparrini, J. Font-Rossello, S. Lannelongue, and C. S. Vallmitjana, “The PARIS concept: An Experimental Demonstration of Sea Surface Altimetry Using GPS Reflected Signals,” *Geoscience and Remote Sensing, IEEE Transactions on*, vol. 39, no. 1, pp. 142–150, 2001.
- [25] M. Martín-Neira, S. D’Addio, C. Buck, N. Floury, and R. Prieto-Cerdeira, “The PARIS Ocean Altimeter In-Orbit Demonstrator,” *Geoscience and Remote Sensing, IEEE Transactions on*, vol. 49, no. 6, pp. 2209–2237, 2011.
- [26] D. Pascual, A. Camps, F. Martín, H. Park, A. Alonso-Arroyo, and R. Onrubia, “Precision bounds in gnss-r ocean altimetry,” *Selected Topics in Applied Earth Observations and Remote Sensing, IEEE Journal of*, vol. 7, pp. 1416–1423, May 2014. DOI: [10.1109/JSTARS.2014.2303251](https://doi.org/10.1109/JSTARS.2014.2303251).
- [27] S. D’Addio, M. Martin-Neira, F. Martín, H. Park, and A. Camps, “Gnss-r altimeter performance: Analysis of cramer-rao lower bounds,” in *2012 Workshop on Reflectometry Using GNSS and Other Signals of Opportunity (GNSS+R)*, 2012, pp. 1–4. DOI: [10.1109/GNSSR.2012.6408258](https://doi.org/10.1109/GNSSR.2012.6408258).
- [28] A. Camps, H. Park, I. Sekulic, and J. M. Rius, “Gnss-r altimetry performance analysis for the geros experiment on board the international space station,” *Sensors*, vol. 17, no. 7, 2017, ISSN: 1424-8220. DOI: [10.3390/s17071583](https://doi.org/10.3390/s17071583). [Online]. Available: <https://www.mdpi.com/1424-8220/17/7/1583>.
- [29] C. Series: *Commercial digital satellite receiver*. <http://www.mil-sat.com/images/cdsr.pdf>.
- [30] V. R. (CLS), J. B. (ESA), S. D. (Space), O. L. (CLS), C. M. (Akka), M. M. (SERCOS), N. P. (CNES), R. E. (isardSAT), A. G.-M. (isardSAT), E. S. (Delft), A. A. (DEIMOS), M. T.-H. (DEIMOS), and M. R. (SERCOS), *Radar altimetry tutorial and toolbox*, <http://www.altimetry.info/radar-altimetry-tutorial/how-altimetry-works/basic-principle/>.
- [31] G. Brown, “The average impulse response of a rough surface and its applications,” *IEEE Transactions on Antennas and Propagation*, vol. 25, no. 1, pp. 67–74, 1977. DOI: [10.1109/TAP.1977.1141536](https://doi.org/10.1109/TAP.1977.1141536).

- [32] J. W. Goodman, “Statistical optics,” *New York, Wiley-Interscience, 1985, 567 p.*, vol. 1, 1985.
- [33] G. A. Hajj and C. Zuffada, “Theoretical description of a bistatic system for ocean altimetry using the GPS signal,” *Radio Science*, vol. 38, no. 5, pp. 1089–1107, 2003.
- [34] J. J. Spilker, “GPS signal structure and performance characteristics,” *Global Positioning System*, vol. 1, pp. 29–54, 1980.
- [35] S. M. Kay, *Fundamentals of Statistical Signal Processing: Estimation Theory*. USA: Prentice-Hall, Inc., 1993, ISBN: 0133457117.
- [36] T. C. for Astronomy Signal Processing and B. Electronics Research (CASPER) - Research group based at the University of California, *Roach2*, <https://casper.berkeley.edu/wiki/ROACH2>.
- [37] B. J. Haines, S. D. Desai, and G. H. Born, “The Harvest Experiment: Calibration of the Climate Data Record from TOPEX/Poseidon, Jason-1 and the Ocean Surface Topography Mission,” *Marine Geodesy*, vol. 33, no. S1, pp. 91–113, 2010.
- [38] S. A. Washburn, B. J. Haines, G. H. Born, and C. Fowler, “The Harvest Experiment LIDAR System: Water Level Measurement Device Comparison for Jason-1 and Jason-2/OSTM Calibration,” *Marine Geodesy*, pp. 277–290, 2011. DOI: [10.1080/01490419.2011.590114](https://doi.org/10.1080/01490419.2011.590114).
- [39] S. SPRL, *Satbeams Web and Mobile. - World of Satellites at your fingertips*, <https://satbeams.com/satellites>.